Master Sciences Technologies Santé

Mention Sciences de la Matière

Spécialité Mécanique, Matériaux, Structures et Procédés

Abradable material removal in aircraft engines: a time delay approach

Presented by:
Nicolas Salvat

Advisors:
Dr. Mathias Legrand (McGill)
Dr. Alain Batailly (McGill)
Dr. Thomas Dupont (ISAT)

Vibrations and Structural Dynamics Laboratory
Faculty of Engineering - McGill University

Université de Bourgogne

UFR des Sciences et Techniques

2010 - 2011

Contents

Forewords

The work presented in this report is the object of a Master's Thesis in order to obtain a double degree: a Mechanical Engineering degree at the Institut Supérieur de l'Automobile et des Transports (ISAT) and a Master's degree in Mechanics, Materials, Structures and Processes at the Université de Bourgogne, both based in Nevers, France.

The project was carried out at McGill University, Montréal, Canada, within the Vibration and Structural Dynamics Laboratory, and focused on building simplified models of the blade/casing interaction observed in modern aircraft engines; phenomenon that occurs when the tip clearance is reduced by introducing an abradable layer on the casing, in order to reach higher compression rates.

The first part of the project focuses in the development of a numerical rod-like blade model that simulates the contact between the blades and the abradable layer, in order to establish wear patterns and analyse the rod's dynamical behavior in different operating conditions. The results obtained are consistent with previous work [2, 3, 24].

This interaction was then considered as a material removal process, which led the way to a brief study of the high speed machining field, specially focussing in the dynamical modeling of the cutting process and its stability analysis. This allowed to model the system by a set of linear Delay Differential Equations (DDEs) that take into account the rod tip displacement at the current revolution as a function of the preceding one.

A stability analysis of the set of DDEs was conducted using two spectral methods: Chebyshev collocation technique and Semi-Discretization Method, which is impossible with more complex models that can only be treated with time integration techniques. The results showed the appearance of critical frequencies and proved that the global stability of the system is strongly dependent on the stability of the rod's first mode.

Keywords: compressor blades, abradable material removal, Delay Differential Equations DDE, stability analysis.

Résumé socio-culturel

Le travail présenté dans ce rapport fait l'objet d'un Mémoire de Master afin d'obtenir un double diplôme: un diplôme d'ingénieur en mécanique des transports de l'Institut Supérieur de l'Automobile et des Transports (ISAT) et un Master Recherche en Mécanique, Matériaux, Structures et Procédés de l'Université de Bourgogne, écoles basées à Nevers, France.

Le projet s'est déroulé à l'Université McGill, située à Montréal, Canada, au sein du Laboratoire de Dynamique des Structures et Vibrations, dirigé par le Prof. Christophe Pierre et le Dr. Mathias Legrand.

Ce laboratoire travaille essentiellement pour l'industrie aéronautique en traitant des problématiques de dynamique de machines tournantes, en particulier ce qui concerne les turboréacteurs des avions modernes. De taille modeste, il compte une dizaine d'employés venant d'horizons très variés, ce qui donne une ambiance de travail plutôt conviviale où chaque personne apporte son expertise afin de faire avancer des projets communs.

En ce qui concerne la ville de Montréal, il s'agit d'une ville très cosmopolite présentant une grande diversité culturelle et sociale, ce qui lui confère un caractère accueillant et dynamique. Ses habitants sont en général serviables et souriants, il est donc facile de s'adapter à cette population ouverte d'esprit et généreuse.

De plus, Montréal est mondialement connue pour ses festivités, car des dizaines de festivals y sont organisés encore une fois faisant preuve d'une grande diversité. En regroupant chanteurs, artistes et acrobates du monde entier, réalisant des spectacles pour la plus part gratuits, c'est une ville vivante tout au long de l'année, même lors des nuits les plus froides de l'hiver!

Résumé technique

Dans le domaine aéronautique, des contraintes de plus en plus sévères, en termes de consommation et rejets de gaz polluants, sont imposées aux constructeurs. C'est pourquoi, l'amélioration du rendement des turboréacteurs est devenu un objectif essentiel des concepteurs.

Plusieurs solutions sont actuellement mises en œuvre, entre autres: (1) la réduction du jeu fonctionnel entre les extrémintés des aubes et le carter, (2) conception de structures plus légères et (3) l'augmentation de la conicité du carter.

La solution (1) est obtenue grâce à une couche de matériau dit *abradable* située sur le carter, ce qui augmente sensiblement les risques de contact entre la partie tournante et la partie fixe, contact qui est maintenant considéré comme faisant partie du fonctionnement normal du moteur.

Cette interaction fait l'objet de ce projet en considérant le déplacement radial des aubes uniquement, pour cette raison celles-ci ont été modélisées par une barre. L'étude se décompose en deux parties:

- Modèle numérique: pour une forme particulière du carter et en mettant en œuvre un algorithme d'intégration temporelle, le contact est géré par une méthode de pénalité et des forces de contact linéaires, directement proportionnelles à la pénétration du sommet d'aube dans la couche d'abradable.

- Modèle analytique: l'interaction aubes/carter pouvant être considéré comme un processus d'enlèvement de matière, des outils de modélisation propres au domaine de l'usinage à grande vitesse ont été utilisés. En considérant une configuration de contact permanent, le système a été modélisé par un ensemble d'équations différentielles à retard linéiares. Une étude de stabilité a été conduite par la suite, en employant deux méthodes spectrales: méthode de Chebyshev et méthode de semi-discrétisation.

L'ensemble de l'étude a permis d'obtenir des résultats en accord avec des travaux précédents [2, 3, 24], et de mettre en avant certains phénomènes liés à cette interaction, tels que: l'apparition de fréquences critiques, la formation de lobes d'usure de la couche de matériau abradable et le fait que la stabilité globale du système est pilotée par la stabilité du premier mode de la barre.

Introduction

McGill University & the laboratory

McGill University is based in Montréal, Canada and it is the oldest university of the city. Founded in 1821, it is nowadays one of the best-known institutions of higher education in the country: ranked among the 20 best universities worldwide, it gathers over 36,000 students from more than 150 countries.

As for the research, McGill is ranked as one of the top research-intensive universities of the country, working in both fundamental and applied sciences, it has made significant contributions not only in health sciences, but also in engineering, computer sciences and social sciences.

Within the Faculty of Engineering, the Vibrations and Structural Dynamics Laboratory is directed by Prof. Christophe Pierre and Dr. Mathias Legrand. The research carried out in this laboratory focuses mainly in linear and non-linear structural dynamics, and more precisely in rotor dynamics, working hand in hand with the aeronautical industry.

Scientific project

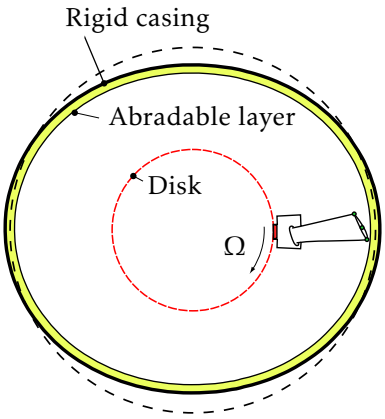

Figure 1: Casing shape [24]

While seeking for better engine performances and higher compression rates in turbomachines, designers of modern aircraft engines usually focus on the following aspects : (1) the reduction of parasitic leakage flows between each stage of the compressor, (2) designing thinner and lighter blades and (3) increasing casing conicity.

Solution (1) is achieved through the reduction of blade tips clearance which is absorbed by a so-called *abradable layer*, as can be seen in Fig. 1. This recent development leads to consider contact between the compressor blade tips and the casing as a part of the engine's normal life.

Work regarding the behavior of the *abradable materials* is currently being carried out at the laboratory and different companies, and has been the subject of several publications [2, 3, 23, 24]. Furthermore, this type of material must be sufficiently strong to withstand gas turbine environment and soft enough to absorb the contact forces without damaging the blades.

A 3D-contact model is being developed, using a plastic law to describe the abradable material removal process and taking into account the most flexible modes of the blade (tension/compression, bending and torsion) using a modal reduction method and a finite element model of the blade and the casing. Different configurations of a statically-distorted casing are also possible to run the simulations, aiming to obtain

suitable abradable properties and operating conditions to avoid large amplitude vibrations of the blades, since it would increase the wear of the abradable layer and considerably reduce the life expectancy of all components.

The first objective of the project was to build a simplified model of the abradable material removal potentially occurring during a rotor/stator interaction to better understand the complex vibratory behavior of the blades using time integration. The model would allow to study the wear of this layer as well as the behavior of the compressor blades in several operating conditions. In this way, specific operating parameters that lead to a stable behavior of the system or on the contrary, to catastrophic scenarios, could be determined.

Not only the wear of the abradable layer can be seen as a material removal process but also there are stability problems in the high speed machining field. The models currently used in this field and their stability analysis led us to the second part of this project: a theoretical study of Delayed Differential Equations (DDEs) using spectral methods.

Chapter 1

Rod/casing interaction

In this chapter a simplified numerical model of the blade/casing interaction is built. The main simplifying assumption is to consider only the radial displacement of the blade (tension-compression) and all flexural displacements are neglected.

To do so, the usual spatial discretization –finite element method– is used, modeling the blade as a rod discretized by a set of *n truss elements* as shown in Fig. 1.1. The rod has a cross-section S and a length L, a Young's modulus E and a density ρ. A penalty

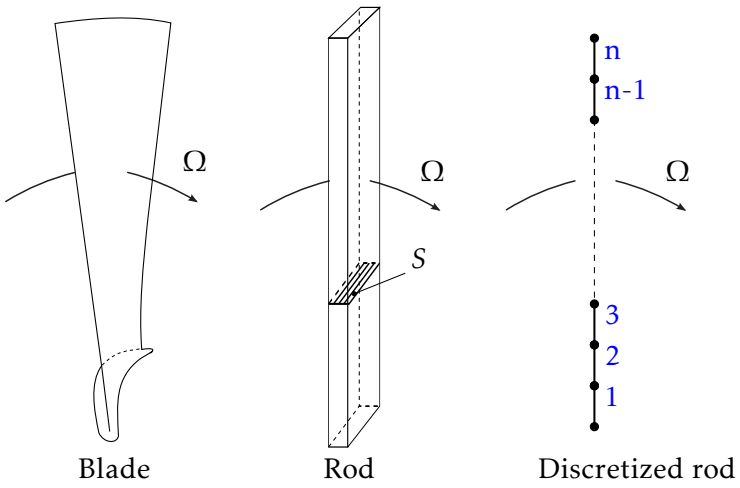

Figure 1.1: Simplified model of the blade

method will be used to describe the contact configuration, *i.e.*, the contact force will be linearly dependent on the penetration of the rod's tip in the abradable layer as will be detailed later on. A time integration algorithm will allow to observe the behavior of the rod as well as the abradable profile after a certain number of revolutions for a given set of operating conditions.

1.1 Rod finite element model

1.1.1 Mass and stiffness matrices

Elementary matrices

The mass and stiffness of the rod illustrated in Fig. 1.1 can be given by the following expressions:

$$m = \rho S L \quad \text{and} \quad k = \frac{ES}{L} \tag{1.1}$$

Discretization into n truss elements yields the following elemetary mass and stiffness:

$$m_e = \rho S l_e \quad \text{and} \quad k_e = \frac{ES}{l_e} \quad \text{with} \quad l_e = \frac{L}{n} \tag{1.2}$$

and the corresponding elementary mass $\mathbf{M}_e$ and stiffness $\mathbf{K}_e$ matrices can be written as follows:

$$\mathbf{M}_e = \frac{m_e}{6}\begin{bmatrix} 2 & 1 \\ 1 & 2 \end{bmatrix} \quad \text{and} \quad \mathbf{K}_e = k_e\begin{bmatrix} 1 & -1 \\ -1 & 1 \end{bmatrix} \tag{1.3}$$

Global matrices

The elementary mass and stiffness matrices given by Eq. (1.3) allow building the global matrices given in Eq. (1.4), which are $(n+1)\times(n+1)$ matrices. Therefore, the size of the system is dependent on the finite element discretization of n truss elements leading to $n+1$ nodes.

$$\mathbf{M} = \frac{m_e}{6}\begin{bmatrix} 2 & 1 & 0 & \dots & & 0 \\ 1 & 4 & 1 & 0 & & \\ 0 & 1 & 4 & 1 & & \vdots \\ \vdots & & \ddots & \ddots & \ddots & 0 \\ & & 0 & 1 & 4 & 1 \\ 0 & & \dots & 0 & 1 & 2 \end{bmatrix}, \quad \mathbf{K} = k_e\begin{bmatrix} 1 & -1 & 0 & \dots & & 0 \\ -1 & 2 & -1 & 0 & & \\ 0 & -1 & 2 & -1 & & \vdots \\ \vdots & & \ddots & \ddots & \ddots & 0 \\ & & 0 & -1 & 2 & -1 \\ 0 & & \dots & 0 & -1 & 1 \end{bmatrix} \tag{1.4}$$

1.1.2 Damping matrix

The modal analysis will allow to calculate the eigenfrequencies and eigenmodes of the rod. A convergence analysis has to be performed to ensure the releability of the proposed spatial discretization.

The steady-state equation of the system can be written from Eq. (1.4) as follows:

$$\mathbf{M}\ddot{\mathbf{q}} + \mathbf{K}\mathbf{q} = \mathbf{0} \tag{1.5}$$

The eigenfrequencies ($\mathbf{D}$) correspond to the eigenvalues of Eq. (1.5), and can be obtained by considering a harmonic response of frequency f:

$$\det(\mathbf{K} - \omega^2\mathbf{M}) = \mathbf{0} \quad \text{with} \quad \omega = 2\pi f \tag{1.6}$$

Solving Eq. (1.6) yields the matrix of eigen pulsations given by the following expression:

$$\mathbf{D} = \begin{bmatrix} \omega_1^2 & & 0 \\ & \ddots & \\ 0 & & \omega_n^2 \end{bmatrix} \tag{1.7}$$

The calculation was ran using the following rod parameters: $E = 210 \cdot 10^7$ Pa, $S = 10 \cdot 10^{-4}$ m^2, $L = 0.5$ m and $\rho = 4600$ Kg/m^3, and with $n = 30$ truss elements, leading to thirty eigenfrequencies. The first five are listed as follows: $f = 338$, 1015, 1694, 2378, and 3069 Hz.

As for the eigenmodes ($\mathbf{V}$), for each eigenfrequency the corresponding eigenvector defined by Eq. (1.8) can be calculated.

$$(\mathbf{K} - \omega_i^2\mathbf{M})\mathbf{v}_i = \mathbf{0}, \quad i = 0, 1...n, \quad \text{and} \quad \mathbf{V} = \begin{bmatrix} \mathbf{v}_0 & \mathbf{v}_1 & \dots & \mathbf{v}_n \end{bmatrix} \tag{1.8}$$

In the modal or frequency domain, the damping matrix ($\mathbf{C}$) can be considered as a diagonal matrix, and each coefficient C_i as linearly dependent on the corresponding eigenfrequency:

$$C_i = 2\xi\omega_i \tag{1.9}$$

where, ξ is the modal damping coefficient. It is important to say that ξ could depend on the eigenfrequency. For the sake of simplicity, $\xi = 0.03$ is constant.

Using Eq. (1.9), the eigenfrequencies given in Eq. (1.7) and the eigenvectors defined in Eq. (1.8), the damping matrix in the space domain reads:

$$\mathbf{C} = 2\xi\mathbf{V}^{-\mathbf{T}}\sqrt{\mathbf{D}}\mathbf{V}^{-\mathbf{1}} \tag{1.10}$$

1.2 Abradable layer model

Once all the matrices necessary to study the dynamical behavior of the system are built, the boundary conditions and the initial abradable layer profile must be defined.

1.2.1 Boundary conditions

Another simplifying assumption is to consider the disk as rigid, which means that the first node of the rod is clamped. This boundary condition is enforced through the compatibility conditions satisfied by the virtual displacement field.

This is simply achieved by removing the rows and columns of the respective degrees of freedom. In this way, the following reduced matrices ($\mathbf{M_r}$ and $\mathbf{K_r}$) of dimension $n \times n$ are defined:

$$\mathbf{M_r} = \frac{m_e}{6}\begin{bmatrix} 4 & 1 & 0 & \dots & 0 \\ 1 & 4 & 1 & & \vdots \\ 0 & \ddots & \ddots & \ddots & 0 \\ \vdots & & 1 & 4 & 1 \\ 0 & \dots & 0 & 1 & 2 \end{bmatrix}, \quad \mathbf{K_r} = k_e\begin{bmatrix} 2 & -1 & 0 & \dots & 0 \\ -1 & 2 & -1 & & \vdots \\ 0 & \ddots & \ddots & \ddots & 0 \\ \vdots & & -1 & 2 & -1 \\ 0 & \dots & 0 & -1 & 1 \end{bmatrix} \tag{1.11}$$

1.2.2 Profile

As for the surrounding abradable layer profile, it is assumed it has an ovoid form (two nodal diameters) in order to absorbe the initial tip clearance, and modeled it with a *blister* function in cylindrical coordinates, as shown in Fig. 1.2. Its diameter is set to 1 m, resulting into a perimeter of approximately 3.14 m. It is important to point out that the rod's tip equilibrium position is 0 along the vertical axis and that with the current model, it will only work in tension-compression along this axis. A more complete model could be built in order to take into account the flexural displacements.

1.3 Wear law

As previously stated, the objective of this section is to build a *wear law* describing the material removal process with a contact force proportional to the rod's tip penetration in the abradable layer. Thus, the contact force F can be written as follows:

$$F = K_e h \tag{1.12}$$

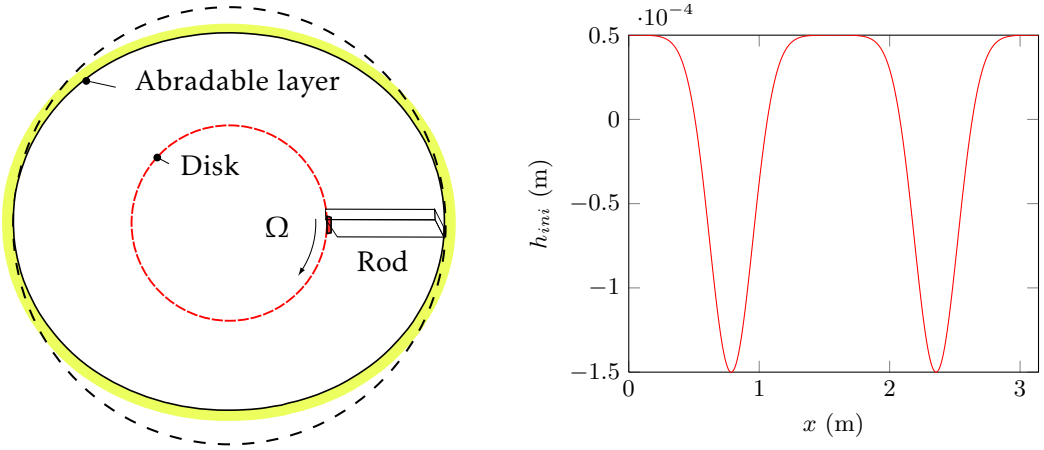

(a) Ovoid abradable layer (b) Blister function

Figure 1.2: Abradable layer initial shape

where K_e is a linear force coefficient in N/m and h is the penetration of the rod in the abradable layer in m. Therefore, h is given by the difference between the rod's tip position and the abradable layer:

$$h(t) = q_{\text{tip}}(t) - h_{\text{ab}} \tag{1.13}$$

where, $q_{\text{tip}}(t)$ is an approximation of the rod's tip displacement from its equilibrium position along the vertical axis at the time t, and h_{ab} corresponds to the abradable layer profile, which is updated after each time iteration.

Finally, if the rod moves beneath the abradable layer, there is no contact and the force must be set to zero. This basic nonlinearity is introduced by testing the sign of $h(t)$: if it is negative, then the force is set to zero:

$$F(t) = \begin{cases} K_e h(t) & \text{if} \quad h(t) > 0 \\ 0 & \text{if} \quad h(t) \leq 0 \end{cases} \tag{1.14}$$

1.4 Solution algorithm

Now that the system has been completely defined and the contact force model chosen, the equation of motion given by the expression (1.15) representing the rod's behavior in time can be solved.

$$\mathbf{M}\ddot{\mathbf{q}} + \mathbf{C}\dot{\mathbf{q}} + \mathbf{K}\mathbf{q} = \mathbf{F} \tag{1.15}$$

with, $\mathbf{F}^{\mathrm{T}} = \begin{pmatrix} 0 & \dots & 0 & F(t) \end{pmatrix}$ and $F(t) = K_e h(t) = K_e(q_{\text{tip}}(t) - h_{\text{ab}})$.

To solve this equation, a center finite difference method is used, leading to the following numerical approximations of the rod's acceleration and speed:

$$\ddot{\mathbf{q}} = \frac{\mathbf{q}_{n+1} - 2\mathbf{q}_n + \mathbf{q}_{n-1}}{\Delta t^2} \quad \text{and} \quad \dot{\mathbf{q}} = \frac{\mathbf{q}_{n+1} - \mathbf{q}_{n-1}}{2\Delta t} \tag{1.16}$$

where Δt is the integration time step, $\mathbf{q}_n$ is an approximation of the rod's displacement at the time t, $\mathbf{q}_{n+1}$ is the approximation at time $t + \Delta t$ and $\mathbf{q}_{n-1}$ is the approximation at time $t - \Delta t$.

By plugging Eq. (1.16) into Eq. (1.15), the following system is obtained:

$$\mathbf{q}_{n+1} = \left(\frac{\mathbf{M_r}}{\Delta t^2} + \frac{\mathbf{C}}{2\Delta t}\right)^{-1} \left[\mathbf{F}_n + \left(\frac{2\mathbf{M_r}}{\Delta t^2} - \mathbf{K_r}\right)\mathbf{q}_n + \left(\frac{\mathbf{C}}{2\Delta t} - \frac{\mathbf{M_r}}{\Delta t^2}\right)\mathbf{q}_{n-1}\right] \tag{1.17}$$

Equation (1.17) will allow to determine the displacement of the rod at each time step, but requires two initial conditions for the first two time steps.

The initial conditions are chosen so that the system is at equilibrium: $\mathbf{q}_1 = \mathbf{q}_2 = \dot{\mathbf{q}}_1 = \dot{\mathbf{q}}_2 = \mathbf{0}$. This way, the following penalty method can be used in order to update the abradable profile:

1. Determine h and the corresponding contact force if $h > 0$.

2. Calculate the rod's displacement $\mathbf{q}_{n+1}$.

3. If a residual penetration is detected, update the profile with the new tip displacement ($h_{\text{ab}} = q^{\text{tip}}_{n+1}$).

As an output, the tip's displacement in time is observed as well as the final abradable layer profile after a certain number of revolutions (*e.g.* $N = 20$ revolutions).

1.5 Results

The aim of this section is to present some of the results that can be obtained with the introduced model. The rotational frequency range is set between 30 Hz and 1500 Hz, which is higher than the usual aircraft engines speed range since the rod is stiffer than a regular blade where flexural motions have lower eigenfrequencies.

After the first set of simulations, the most important displacements and consequently, the most important wear of the abradable layer, took place at rotational frequencies f_Ω that are even dividers of the rod's first eigenfrenquency ($f_1 = 338$ Hz):

$$f_\Omega = \frac{f_1}{k} \quad \text{with} \quad k = 2, 4, 6\ldots \tag{1.18}$$

These frequencies are often called *critical frequencies*. After this first eigenfrequency f_1, no major wear phenomena were observed.

The 2-nodal diameters of the abradable layer produce an interaction for even dividers of f_1 which explains the above observation. If an odd number of nodal diameters or a combination of even and odd nodal diameters is considered, odd dividers k may have significant contributions to the wear phenomenon.

1.5.1 Abradable profile

As seen in Fig. 1.3, a map of the final abradable profile as a function of the rotational frequency f_Ω and the linear position of the casing after 20 revolutions is plotted. Figures 1.3 and 1.4 clearly show the different critical frequencies with the appearance of wear lobe patterns and large amplitude vibrations. Furthermore, the nonlinearity of the contact and wear phenomena slightly increase these critical frequencies, this is called *contact stiffening*. Consequently, when Eq. (1.18) is almost satisfied, critical behaviors are expected.

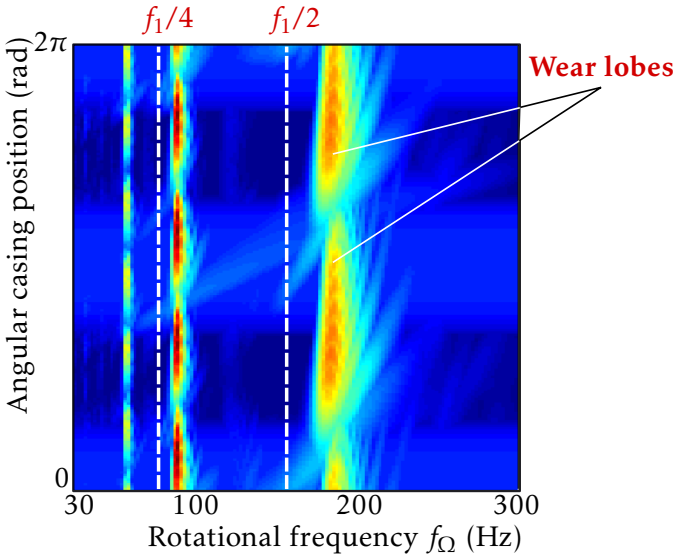

Figure 1.3: Abradable layer profile after 20 revolutions

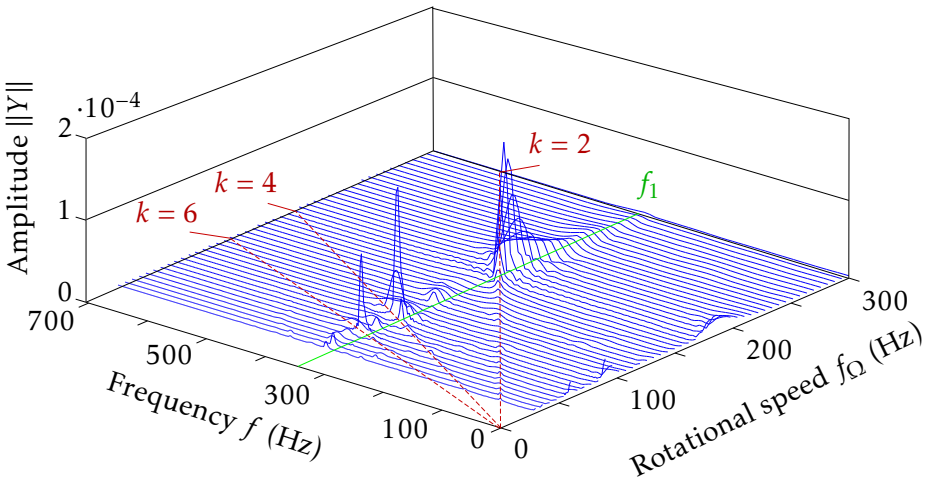

Figure 1.4: Spectrum of the rod's response

1.5.2 Frequency domain

As for the frequency content of the rod's response represented by Fig. 1.4, a Fourier Transform was used in order to plot the amplitude of the rod's tip vibrations as a function of their frequency and the rotational speed.

Figure 1.4 is in perfect agreement with the wear map drawn in Fig. 1.3, since large amplitude vibrations are observed at the corresponding critical rotational frequencies. One can also show the so-called *engine orders*, defined as:

$$f = k f_\Omega \quad \text{with} \quad k = 1, 2, 3 \ldots \tag{1.19}$$

With this definition, we can state that the maximum amplitude vibrations are expected at the intersection of the different engine orders and the rod's first eigenfrequency f_1 slightly shifted. These complex behaviors and results are consistent with those presented in previous work [2, 3, 24], and pave the way to more complex simulations, in particular to introduce other types of contact forces and consider flexural displacements of the blade.

In addition, since the blade/casing interaction can be seen as a material removal process, an overview of the high speed machining field will be given in the next chapter, focusing in particular in the dynamics of the cut and its stability analysis.

This will allow to use a similar mathematical background and apply different analytical techniques to analyze the stability of the proposed model.

Chapter 2

High speed machining

This chapter features a brief introduction to the main industrial machining processes – turning and milling – with a review of cutting mechanics and a description of the usual associated modeling. This will allow to draw an analogy with our topic of interest and lay the foundations of the numerical models developed later on.

Generally speaking, machining processes are associated with the principle of material removal and so are turning and milling. However, a major difference exists between these two processes. Indeed, in the turning process the workpiece rotates and the cutter (tool) translates to generate the cut whereas in the milling process the cutter rotates while the workpiece translates.

Several studies [9, 14, 19, 39] show that different combinations of the cutting parameters, such as, the depth of cut, the rotational spindle speed or the radial engagement, may lead to instabilities during the cutting process and to self-excited vibrations of the cutter. This phenomenon is called *chatter* and will be detailed later on as well as the advances on stability prediction in this field.

2.1 Cutting mechanics

The cutting process in machining has been a subject of interest in the industry for a long time [28, 29], not only to determine the appropriate operating parameters to obtain a smooth surface, but also to reduce the wear of the cutter as well as the power required to make the cut. Even if there have been more sophisticated studies to model these forces [26], in general, machinists consider the following tangential (F_t) and radial (F_r) forces represented in Fig. 2.1:

$$F_t = K_t b h \tag{2.1}$$

$$F_r = K_r b h \tag{2.2}$$

where, b is the nominal depth of cut, h is the instantaneous chip thickness, K_t and K_r are linearised cutting coefficients dependents on the workpiece material, they are also called *Specific Force coefficients* and represent the force required to remove a chip which surface is 1 mm^2.

Equation (2.2) can be written as a function of the tangential force as follows:

$$F_r = k_r F_t \quad \text{where} \quad k_r = K_r / K_t \tag{2.3}$$

Other ways of modeling the cutting forces can be found in the literature :

1. Cubic polynomial approximation [12] :

$$F_t = b(\rho_1 h + \rho_2 h^2 + \rho_3 h^3) \tag{2.4}$$

2. Linear threshold approximation [13, 39] :

$$F_t = b(K_0 + K_s h) \tag{2.5}$$

3. Exponential approximation [20] :

$$F_t = K_e b h^p \tag{2.6}$$

All the coefficients used in equations (2.4), (2.5) and (2.6) are empirical and are dependent on the material of the workpiece. Furthermore, equation (2.3) is still valid for any kind of approximation.

2.2 Machining dynamics

Much like for the cutting mechanics, understanding the dynamics of the different machining processes has been a topic of interest in the industry, since they are strongly linked to the stability of the cut [33, 37, 39]: a stable cut means that the vibrations between tool and workpiece decay in time, and on the contrary, it is an unstable cut when the oscillations grow.

In this chapter, an overview of the dynamical modeling of turning and milling is presented, as well as a description of the cutting motion of each process, since depending on the type of process, the cutting motion will be different.

2.2.1 Turning

The turning process is a single-point tool operation, which means that the tools have a single cutting edge. Often used to describe other machining operations like *boring* and *shaping* which are also single-point tool operations, it is the oldest and most commonly used machining process in the industry.

It is used for machining axisymetric parts since the workpiece rotates in a spindle with a rotational speed Ω, specified in rpm or in rad/s. The cutter moves with such a *feed rate* that it travels the feed f_r in one revolution of the workpiece, and its movement can be either parallel or perpendicular to the spindle axis in order to generate the desired surface. As shown in Fig. 2.1, a straight side-cutting tool generates

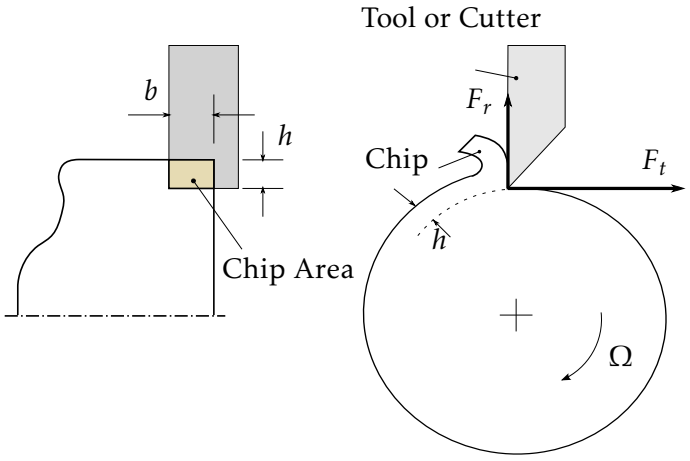

Figure 2.1: Cutting process in turning; constant chip width

a chip depending on the depth of cut b and the feed rate. Furthermore, in this case

we can consider a constant instantaneous chip thickness h will equal to the feed rate ($h = h_{av} = f_r$).

As previously stated, the area of the chip will determine the amplitude of the cutting force.

2.2.2 Milling

The milling process is somewhat more complex than turning since it is a multi-point tool operation. The cut is generated by the rotation of a multi-toothed tool and the translation of the workpiece in different directions.

The rotational speed Ω of the tool is called the *spindle speed*, and the translational motion of the workpiece is given by the *linear feed rate* f, specified in $\text{mm} \cdot \text{min}^{-1}$. The *feed per tooth* f_t, also called *chip load* in $\text{mm} \cdot \text{min}^{-1} \cdot \text{tooth}^{-1}$ and shown in Fig. 2.2,

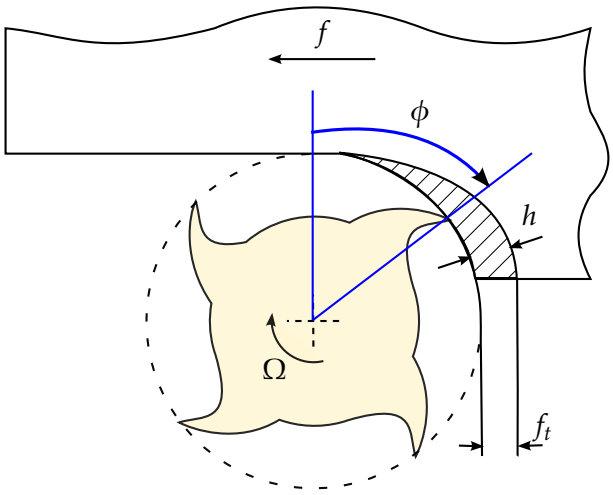

Figure 2.2: Cutting process in milling & periodic chip variation

determines the variation of the chip thickness depending on the cutting angle ϕ:

$$f_t = \frac{f}{N_t \Omega} \quad \text{and} \quad h = f_t \sin(\phi) \tag{2.7}$$

Therefore, during the milling process, each tooth of the cutter is subjected to a periodic variation of the cutting force, unlike in turning, where this force is constant.

The case represented in Fig. 2.2 is called *down-milling* and the force varies from zero to its maximum (*e.g.* $F = K_s b f_t$). On the contrary, if the the spindle speed is inverted, with the appropriate cutter, the process is called *up-milling* and the cutting force varies from its maximum to zero.

2.3 Chatter and stability prediction

As previously stated, chatter is a self-excited type of vibrations that occurs during the cutting process if the chip width becomes too large. It has been observed and studied for several decades [40, 41]. It leads to a variation of the cutting force and the instantaneous chip thickness, resulting in wavy and uneven surfaces as shown in Fig. 2.3. Therefore, this phenomenon is considered as unacceptable in the machining process. Chatter may arise from two main physical phenomena:

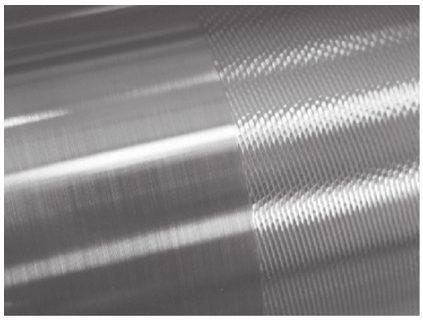

Figure 2.3: Chatter marks in turning

Mode coupling: this phenomenon occurs when vibration modes of the workpiece and the tool are close. It results from the relative vibration between the tool and the workpiece, leading to an elliptical movement of the cutter. This interaction can only exist when the workpiece is sufficiently flexible, for example in finish milling operations of thin walled structures.

Regeneration of waviness: this is the most common physical phenomenon leading to self-excited type of vibrations in metal cutting. If there are relative vibrations between the tool and the workpiece during a pass, a wavy surface is generated during the cut. Since the chip is removed from a surface that was produced during the preceding revolution in turning and by the previous tooth of the cutter in milling, once the waviness appears, it creates a variation of the instantaneous chip thickness and consequently, a variation of the cutting force, inducing more vibrations and the newly created surface is wavy again.

Chatter can be accounted for by using a set of Delay-Differential Equations (DDEs) based on the models established in section 2.2. DDEs allow to take into consideration the vibration of the tool at the current pass as well as the previous pass, as shown in Fig. 2.4.

Considering this single degree of freedom (SDoF) model, where q represents the tool displacement, one can write the following equation of motion:

$$m\ddot{q}(t) + c\dot{q}(t) + kq(t) = F(t) \tag{2.8}$$

If we consider a linear model of the cutting force, equation (2.12) becomes:

$$m\ddot{q}(t) + c\dot{q}(t) + kq(t) = K_r bh(t) \quad \text{and} \quad h(t) = h_0 + q(t-\tau) - q(t) \tag{2.9}$$

As shown in section 2.2, the average thickness h_0 depends on the machining process. In turning, it is the average chip thickness ($h_0 = h_{av}$) whereas in milling, it depends on the cutter angle ϕ and the chip load f_t ($h_0 = f_t \sin(\phi)$). As for the time delay τ, it represents the time for one rotation in turning and the tooth pass period in milling:

$$\tau = \frac{2\pi}{N_t \Omega} \tag{2.10}$$

where N_t is the number of teeth on the cutter.

Equation (2.12) can be generalized to a 2 Degrees of Freedom (2-DoF) system, by using displacement $\mathbf{q}$ and force $\mathbf{F}$ vectors, the stiffness matrix $\mathbf{K}$, the damping matrix $\mathbf{C}$ and the mass matrix $\mathbf{M}$, as follows:

$$\mathbf{M}\ddot{\mathbf{q}} + \mathbf{C}\dot{\mathbf{q}} + \mathbf{K}\mathbf{q} = \mathbf{F}, \tag{2.11}$$

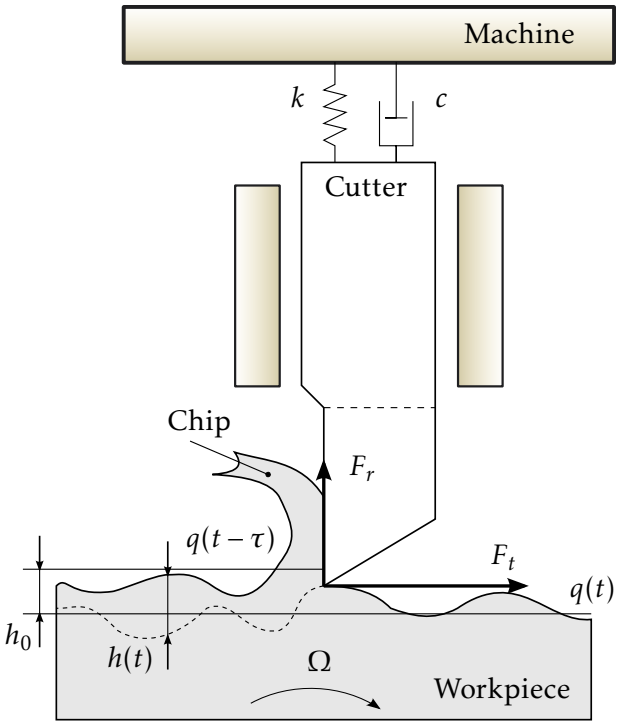

Figure 2.4: Model of chip thickness variation due to tool vibration [12]

with:

$$\mathbf{M} = \begin{bmatrix} m_1 & 0 \\ 0 & m_2 \end{bmatrix}, \quad \mathbf{K} = \begin{bmatrix} k_1 & 0 \\ 0 & k_2 \end{bmatrix}, \quad \text{and} \quad \mathbf{C} = \begin{bmatrix} c_1 & 0 \\ 0 & c_2 \end{bmatrix}$$

and the displacement and cutting force vectors can be written as follows:

$$\mathbf{q} = \begin{pmatrix} q_1 \\ q_2 \end{pmatrix} \quad \text{and} \quad \mathbf{F} = \begin{pmatrix} F_1 \\ F_2 \end{pmatrix}$$

In order to better understand this phenomenon as well as the use of DDEs, a 1-DoF numerical model of the turning process was built using a linear cutting force:

$$m\ddot{y}(t) + c\dot{y}(t) + ky(t) = K_r b(h_0 + y(t-\tau) - y(t)) \tag{2.12}$$

For this program different numerical time-integration algorithms were used: explicit Euler integration [39], finite difference and MATLAB `dde23` function. In all cases the same results in terms of tool displacement and cutting forces were obtained. Figure 2.5 represents the tool motion in both stable and unstable cutting conditions.

Rather than using time-domain simulations, it is simpler to treat the set of DDEs in the Laplace domain since the delayed term becomes an exponential function. What is usually done in order to study the stability of the system is to work on the Frequency Response Functions, easily built in the Laplace domain and analyzing the ratio between the instantaneous chip thickness and its mean value.

This method allows to obtain the characteristic equation of the system and analyze its stability depending on the sign of its root's real part:

- Positive real part: vibrations grow and the system is unstable.
- Negative real part: vibrations decay and the cut is considered as stable.

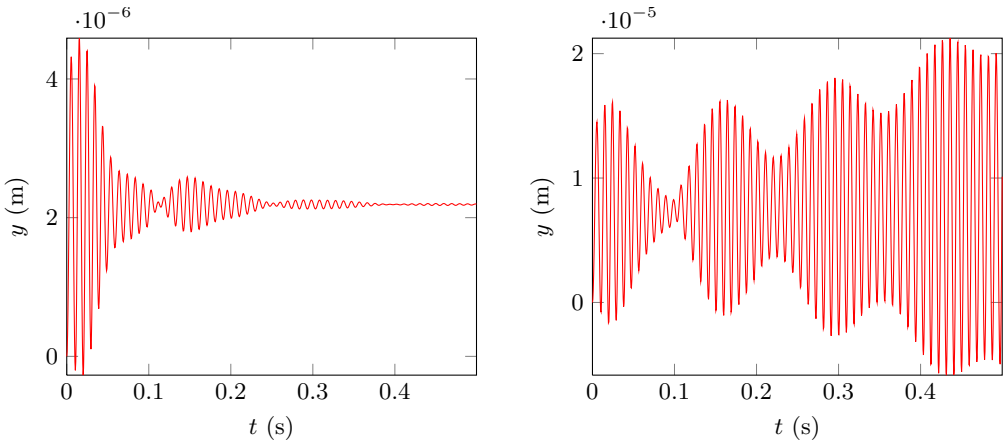

(a) Stable tool motion (b) Unstable tool motion

Figure 2.5: Chatter simulation in turning [39]

- The boundary between stable and unstable behaviors is represented by the roots with zero real part.

Studies show that the most influent parameter is the depth of cut. By calculating its values that result into a zero real part root of the characteristic equation b_{lim} for different rotational speeds, we obtain the boundary of stability of the system: the cut will be stable for $b < b_{\text{lim}}$ and unstable for $b > b_{\text{lim}}$. One is then able to draw the so-called *Stability Lobes Diagram* (SLD) shown in Fig. 2.6.

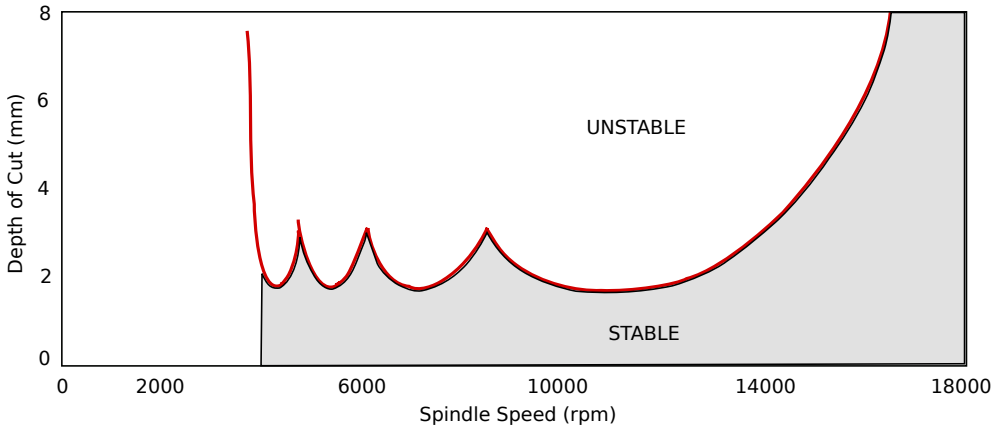

Figure 2.6: SLD example [15]

There have been many studies regarding the stability prediction of milling and turning processes, and despite the advances in the numerical modeling and the experimental verifications, it is still a topic with many unknowns, especially regarding the bifurcation phenomenon from which chatter appears.

Some original work has been done considering nonlinear dynamics [10, 36, 37], multi-mode dynamics [38] and state-dependent delays [20], using Finite Element Methods (FEM) [15, 27] or Full Discretization Methods (FDM) [16, 44], all of them with the purpose of controlling the cutting parameters in order to avoid chatter. Most of these works use frequency based analysis, but time domain simulations are increasingly being used [4, 25, 34].

Generally speaking, DDEs are commonly used and allow to reproduce complex vibratory behaviors and make global stability analysis of the cutter/workpiece interaction, even if the cutting force is often considered as linearly dependent on the chip area, results promise significant advances in the field.

In the next chapters the system will be modeled by a set of DDEs in order to use analytical methods to study its stability, and see if any particular behaviors may emerge. This will allow to have a global picture of the rod's behavior without having to use time-integration techniques.

Chapter 3

Theoretical study of a DDE

The analysis of Delay Differential Equations (DDEs) has been a subject of interest for years in many different fields, such as, control theory, telecommunications, neural networks, biology, population dynamics, and many others. Several books have been published regarding the dynamics of time delayed systems [22, 30], or dealing with more theoretical aspects of the DDEs [11, 32].

This chapter essentially focuses on modeling the rod/casing interaction by a set of DDEs and presenting a stability analysis [35] of the system. An eigenvalue-based approach will be used with the comparison of two spectral methods: *Chebyshev collocation method* (section 3.2) and *Semi-Discretization Method* (SDM) (section 3.3). For the sake of simplicity, only a linear contact force model will be used.

3.1 General principle of stability analysis

The stability analysis of a DDE is challenging because the associated eigenvalue problem is infinite-dimensional, whereas for Ordinary Differential Equations (ODEs) it is finite-dimensional.

Let us consider a delayed system with a single and constant delay τ:

$$\begin{aligned} \dot{\mathbf{Z}}(t) &= \mathbf{A}\mathbf{Z}(t) + \mathbf{B}\mathbf{Z}(t-\tau) \\ \mathbf{Z}(t) &= \varphi(t), \quad t \in [-\tau\,;0] \end{aligned} \tag{3.1}$$

where, A and B are constants, and φ is a function defined as initial conditions in the interval $[-\tau\,;0]$.

We assume an exponential *anzatz* solution in the same way as for ODEs, such as:

$$\mathbf{Z}(t) = \mathbf{Z}_0 \exp(\lambda t) \tag{3.2}$$

Plugging Equation (3.2) into Equation (3.1) yields:

$$\det(\lambda \mathbf{I} - \mathbf{A} - \mathbf{B}exp(-\lambda\tau)) = 0 \tag{3.3}$$

Equation (3.3) is the characteristic equation of the DDE and is known as a *nonlinear eigenvalue problem*. Due to the exponential term, it has an infinite number of solutions.

Solving this type of equation has given rise to several methods [21, 43], basically divided into two groups: the *Solution Operator Discretization* (SOD) and the *Infinitesimal Generator Discretization* (IGD), both based on a rational or polynomial approximation of the exponential term, making the characteristic equation finite-dimensional and easier to solve.

Other methods focus on building a so-called *monodromy operator* or *transition matrix* $\mathbf{\Phi}$ allowing to determine the state of the system at a time t_i based on the state of the system at the delayed time $t_i - \tau$: $(\mathbf{Z}(t_i) = \mathbf{\Phi}\mathbf{Z}(t_i - \tau))$.

In order to use these methods to study the stability of the rod/casing interaction, the system must be modeled as a set of DDEs. To do so, the principal assumption that has to be made is to consider a permanent contact configuration.

In this way, the contact force will no longer be dependent on the abradable layer shape, but only on the position of the rod's tip at the current and previous revolutions as defined in the following expression:

$$\mathbf{F}^{\mathrm{T}} = \begin{pmatrix} 0 & \dots & 0 & F(t) \end{pmatrix} \text{ and } F(t) = K_e h(t) = K_e(q_{\mathrm{tip}}(t-\tau) - q_{\mathrm{tip}}(t)) \tag{3.4}$$

Furthermore, the set of DDEs must be expressed in the modal domain of the underlying linear system. This will enable us to study the contribution of each vibration mode of the structure to the dynamic stability of the system.

Therefore, Equation (1.15) projected in the modal domain using the contact force defined in Equation (3.4) and the eigenvectors ($\mathbf{V}$) defined in expression (1.8) yields:

$$\mathbf{V}^{\mathrm{T}}\mathbf{M}\mathbf{V}\ddot{\mathbf{u}}(t) + \mathbf{V}^{\mathrm{T}}\mathbf{C}\mathbf{V}\dot{\mathbf{u}}(t) + \mathbf{V}^{\mathrm{T}}\mathbf{K}\mathbf{V}\mathbf{u}(t) = \boldsymbol{\kappa}(\mathbf{u}(t-\tau) - \mathbf{u}(t)) \tag{3.5}$$

with,

$$\mathbf{V}\mathbf{u} = \mathbf{q} \quad \text{and} \quad \boldsymbol{\kappa} = \mathbf{V}^{\mathrm{T}} \begin{bmatrix} 0 & \dots & 0 & 0 \\ \vdots & \ddots & \vdots & \vdots \\ 0 & \dots & 0 & 0 \\ 0 & \dots & 0 & K_e \end{bmatrix} \mathbf{V}$$

where K_e is a linear specific force coefficient as defined in Equation (1.12). Orthogonality properties of the eigenvectors and scaling them to the mass of the system, the following expressions can be written:

$$\mathbf{V}^{\mathrm{T}}\mathbf{M}\mathbf{V} = \mathbf{I}_n = \begin{bmatrix} 1 & & 0 \\ & \ddots & \\ 0 & & 1 \end{bmatrix} \quad \text{and} \quad \mathbf{V}^{\mathrm{T}}\mathbf{K}\mathbf{V} = \mathbf{D} = \begin{bmatrix} \omega_1^2 & & 0 \\ & \ddots & \\ 0 & & \omega_n^2 \end{bmatrix} \tag{3.6}$$

since the damping matrix is already defined in the modal domain in Equation (1.10), $\mathbf{V}^{\mathrm{T}}\mathbf{C}\mathbf{V}$ simply yields into:

$$\mathbf{V}^{\mathrm{T}}\mathbf{C}\mathbf{V} = 2\xi\sqrt{\mathbf{D}} = 2\xi \begin{bmatrix} \omega_1 & & 0 \\ & \ddots & \\ 0 & & \omega_n \end{bmatrix} \tag{3.7}$$

Accordingly, Equation (3.5) simplifies as:

$$\mathbf{I}\ddot{\mathbf{u}}(t) + 2\xi\sqrt{\mathbf{D}}\dot{\mathbf{u}}(t) + \mathbf{D}\mathbf{u}(t) = \mathbf{\Phi}(\mathbf{u}(t-\tau) - \mathbf{u}(t)) \tag{3.8}$$

Most of the spectral methods used to study the stability of DDEs are applied to first order equations. Therefore, one must define a state vector allowing to transform de second order DDE (3.8) into a first order one.

Let $\mathbf{Z}$ be a state vector such that $\mathbf{Z}^{\mathrm{T}}(t) = \begin{pmatrix} \mathbf{u}(t) & \dot{\mathbf{u}}(t) \end{pmatrix}$. By introducing this state vector, one can rewrite Equation (3.8) as a first order system as defined in Equation (3.1), with:

$$\mathbf{A} = \begin{bmatrix} \mathbf{0}_n & \mathbf{I}_n \\ -\mathbf{D} - \mathbf{\Phi} & -2\xi\sqrt{\mathbf{D}} \end{bmatrix} \quad \text{and} \quad \mathbf{B} = \begin{bmatrix} \mathbf{0}_n & \mathbf{0}_n \\ \mathbf{\Phi} & \mathbf{0}_n \end{bmatrix} \tag{3.9}$$

The coefficients defined in Equation (3.9) are constant in our particular case and of size $2n \times 2n$, size which is dependent on the spatial discretization of the rod.

3.2 Chebyshev collocation method

This discretization method is based on the construction of a differentiation matrix, which is then used to differentiate the set of DDEs [42] and build an approximation of the *monodromy operator*, as will be shown later. It has been successfully used by several authors, in particular [5–8] have used it to compute Stability Lobes Diagrams (SLD) in milling and discuss the stability of a damped delayed Mathieu equation.

In order to apply this method, one needs to define an unevenly spaced grid called *Chebyshev points*, which are defined by expression (3.10) and can be represented geometrically by Fig. 3.1.

$$x_j = \cos(j\pi/m) \quad \text{where} \quad j = 0, 1 \dots m, \tag{3.10}$$

This unevenly spaced grid allows the construction of *Chebyshev polynomials* so that

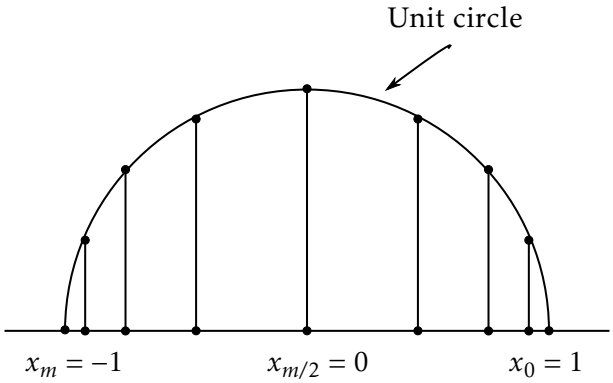

Figure 3.1: Geometrical representation of Chebyshev points

$T_j(x_j) = \arccos(jx_j)$, which is a complete basis set defined in the interval $[-1\,;1]$ where a function $f(x)$ can be expressed as:

$$f(x) = \sum_{j=0}^{\infty} a_j T_j(x) \tag{3.11}$$

The so-called *Chebyshev differentiation matrix* $\mathbf{D}_m$ is then computed using MATLAB's `cheb.m` routine [42, chp.6] with $m+1$ Chebyshev nodes. Therefore, $\mathbf{D}_m$ is an $(m+1)\times(m+1)$ matrix so that:

$$(\mathbf{D}_m)_{00} = \frac{2m^2+1}{6}, \qquad (\mathbf{D}_m)_{mm} = -\frac{2m^2+1}{6},$$
$$(\mathbf{D}_m)_{jj} = \frac{-x_j}{2(1-x_j^2)}, \qquad j = 1, 2, \dots, m-1,$$
$$(\mathbf{D}_m)_{ij} = \frac{c_i}{c_j}\frac{(-1)^{i+j}}{(x_i - x_j)}, \qquad i \neq j, \quad i, j = 0, \dots, m,$$
$$\text{with} \quad c_i = \begin{cases} 2, & \text{if } i = 1 \text{ or } m \\ 1, & \text{otherwise.} \end{cases}$$

The computation is performed by default in the interval $[-1\,;1]$ where Chebyshev polynomials are defined, but since the set of DDEs is defined in the interval $[-\tau\,;\tau]$, $\mathbf{D}_m$ must be *shifted* by multiplying it by $2/\tau$.

As shown in [8], one can build another differentiation matrix $\mathbf{D_N}$ by using the *Kronecker product* of $\mathbf{D}_m$ matrix and the identity matrix $\mathbf{I}_{2n}$ of size $2n \times 2n$ in order to scale it to the size of the desired system:

$$\mathbf{D_N} = \mathbf{D}_m \otimes \mathbf{I}_{2n} \tag{3.12}$$

where $\mathbf{D_N}$ will be a $2n(m+1) \times 2n(m+1)$ differentiation matrix that will be used to differentiate the state vector $\mathbf{Z}(t)$, so that $\dot{\mathbf{Z}}(t) = \mathbf{D_N}\mathbf{Z}(t)$.

First, let $\{\varphi_i\}$ be a set of values of the initial function $\varphi(t)$ in the interval $[-\tau\,;0]$, and $\{Z_i\}$ be a set of values of the solution function $\mathbf{Z}(t)$, at the shifted Chebyshev collocation points in the interval $[0\,;\tau]$. The nodes are ordered right to left as shown in Fig. 3.1. An approximation of the monodromy operator can be defined by $\mathbf{\Phi}$, such that $\{Z_i\} = \mathbf{\Phi}\{\varphi_i\}$ and taking into account the matching condition at $t = 0$, $Z_m = \varphi_1$. To do so, Equation (3.1) must be rewritten in the collocation approximation form as follows:

$$\begin{aligned} &\mathbf{Z}(t) \to \{\mathbf{Z}_j\}; \quad \mathbf{Z}(t-\tau) \to \varphi(t) \to \{\boldsymbol{\varphi}_j\}; \quad \dot{\mathbf{Z}}(t) \to \{\dot{\mathbf{Z}}_j\} \\ &\hat{\mathbf{D}}_\mathbf{N}\{Z_i\} = \hat{\mathbf{M}}_\mathbf{A}\{Z_i\} + \hat{\mathbf{M}}_\mathbf{B}\{\varphi_i\} \end{aligned} \tag{3.13}$$

where:

$$\hat{\mathbf{M}}_\mathbf{A} = \begin{bmatrix} \mathbf{A} & \mathbf{0}_{2n} & \dots & & \mathbf{0}_{2n} \\ \mathbf{0}_{2n} & \mathbf{A} & & & \vdots \\ \vdots & & \ddots & & \\ \mathbf{0}_{2n} & \dots & \mathbf{0}_{2n} & \mathbf{A} & \mathbf{0}_{2n} \\ \mathbf{0}_{2n} & & \dots & & \mathbf{0}_{2n} \end{bmatrix}, \qquad \hat{\mathbf{M}}_\mathbf{B} = \begin{bmatrix} \mathbf{B} & \mathbf{0}_{2n} & \dots & & \mathbf{0}_{2n} \\ \mathbf{0}_{2n} & \mathbf{B} & & & \vdots \\ \vdots & & \ddots & & \\ \mathbf{0}_{2n} & \dots & \mathbf{0}_{2n} & \mathbf{B} & \mathbf{0}_{2n} \\ \mathbf{I}_{2n} & \mathbf{0}_{2n} & \dots & & \mathbf{0}_{2n} \end{bmatrix} \tag{3.14}$$

and $\hat{\mathbf{D}}_\mathbf{N}$ is obtained from $\mathbf{D_N}$ by replacing the last $2n$ rows by $[\mathbf{0}_{2n} \dots \mathbf{0}_{2n}\, \mathbf{I}_{2n}]$, where $\mathbf{0}_{2n}$ and $\mathbf{I}_{2n}$ are the null and identity matrices of size $2n \times 2n$, respectively. This modification allows to take into account the matching condition defined above, *i.e.*, $Z_m = \varphi_0$. Once $\hat{\mathbf{D}}_\mathbf{N}$, $\hat{\mathbf{M}}_\mathbf{A}$ and $\hat{\mathbf{M}}_\mathbf{B}$ are computed, the approximation of the monodromy operator can simply be defined as:

$$\mathbf{\Phi} = [\hat{\mathbf{D}}_\mathbf{N} - \hat{\mathbf{M}}_\mathbf{A}]^{-1}\hat{\mathbf{M}}_\mathbf{B} \tag{3.15}$$

The stability analysis of the solution $\mathbf{Z}(t) = \mathbf{0}$ is then based on *Floquet theory*, *i.e.*, if the modulus of the eigenvalues of the monodromy operator (*Floquet multipliers*) is less than one, the solution is stable. On the contrary, if at least one eigenvalue is greater than one in modulus, the solution will be unstable.

Therefore, the limit of the system's stability can be defined for a set of parameters (rotational speed and specific force coefficient) that yield into an eigenvalue equal to one in modulus.

3.3 Semi-discretization method

The Semi-Discretization Method (SDM) is a well known numerical method used in several fields such as, finite element analysis or computational fluid mechanics, and it has been successfully used for the stability analysis of linear time-delayed systems [16–18].

Much like Chebyshev collocation technique, the aim of SDM is to build a transition matrix or monodromy operator in order to compute its eigenvalues and use Floquet theory to analyze the stability of the system. The discretization is constructed over one

period time interval T, such that $T = k\Delta t$, where Δt is the length of the interval $[t_i\,; t_{i+1}]$, $i = 0, 1\ldots$ In our case the time period is chosen to be equal to the time delay $T = \tau$. In this way, for a sufficiently small time step Δt, Equation (3.1) can be approximated as (for details see [17, 18]):

$$\dot{\mathbf{Z}}(t) = \mathbf{A}\mathbf{Z}(t) + \mathbf{B}\mathbf{Z}_{\tau,i} \tag{3.16}$$

where, $\mathbf{Z}_{\tau,i}$ is a weighted linear combination of the delayed discrete values $\mathbf{Z}_{i-k}$ and $\mathbf{Z}_{i-k+1}$:

$$\mathbf{Z}_{\tau,i} = w_a\mathbf{Z}_{i-k+1} + w_b\mathbf{Z}_{i-k} \approx \mathbf{Z}(t-\tau) \tag{3.17}$$

This discretization trick allows to treat the delayed term as a constant and build a general analytical solution of Equation (3.16) since it can be treated as a regular ordinary differential equation. Therefore, for an initial condition $\mathbf{Z}(t_i) = \mathbf{Z}_i$, the solution reads:

$$\mathbf{Z}(t) = \exp(\mathbf{A}_i(t-t_i))(\mathbf{Z}_i + \mathbf{A}_i^{-1}\mathbf{B}_i\mathbf{Z}_{\tau,i}) - \mathbf{A}_i^{-1}\mathbf{B}_i\mathbf{Z}_{\tau,i} \tag{3.18}$$

By using Equation (3.17) and substituting t by t_{i+1} so that $\mathbf{Z}(t_{i+1}) = \mathbf{Z}_{i+1}$, Equation (3.16) yields:

$$\mathbf{Z}_{i+1} = \mathbf{P}_i\mathbf{Z}_i + w_a\mathbf{R}_i\mathbf{Z}_{i-k+1} + w_b\mathbf{R}_i\mathbf{Z}_{i-k} \tag{3.19}$$

with:

$$\mathbf{P}_i = \exp(\mathbf{A}_i\Delta t) \quad \text{and} \quad \mathbf{R}_i = (\exp(\mathbf{A}_i\Delta t) - \mathbf{I}_{2n})\mathbf{A}_i^{-1}\mathbf{B}_i \tag{3.20}$$

Based on this solution, one can build a discrete map by defining a $(n(k+1)\times 1)$ state vector $\mathbf{Y}_i^{\mathrm{T}} = \begin{pmatrix}\mathbf{u}_i & \dot{\mathbf{u}}_i & \mathbf{u}_{i-1} & \mathbf{u}_{i-2} & \cdots & \mathbf{u}_{i-k}\end{pmatrix}$ so that:

$$\mathbf{Y}_{i+1} = \mathbf{D}_{\mathbf{S},i}\mathbf{Y}_i \tag{3.21}$$

with:

$$\mathbf{D}_{\mathbf{S},i} = \begin{bmatrix} \mathbf{P}_{1\ldots n,i} & \mathbf{P}_{n+1\ldots 2n,i} & \mathbf{0}_n & \cdots & \mathbf{0}_n & w_a\mathbf{R}_{1\ldots n,i} & w_b\mathbf{R}_{1\ldots n,i} \\ \mathbf{I}_n & \mathbf{0}_n & \mathbf{0}_n & \cdots & & \mathbf{0}_n & \mathbf{0}_n \\ \mathbf{0}_n & \mathbf{0}_n & \mathbf{I}_n & & & \mathbf{0}_n & \mathbf{0}_n \\ \vdots & & & \ddots & & & \vdots \\ \mathbf{0}_n & \mathbf{0}_n & & & \mathbf{I}_n & \mathbf{0}_n & \mathbf{0}_n \\ \mathbf{0}_n & \mathbf{0}_n & \cdots & & \mathbf{0}_n & \mathbf{I}_n & \mathbf{0}_n \end{bmatrix} \tag{3.22}$$

where $\mathbf{P}_{1\ldots n,i}$ denotes the 1 to n columns of $\mathbf{P}_i$. Note that only the first n columns of matrix $\mathbf{R}_i$ are taken into account: the last n columns of matrix $\mathbf{B}_i$ are zeros since the system studied is not of neutral type, *i.e.*, there are no delayed terms in speed in the set of DDEs. An approximation of the monodromy operator can then be built as a *transition matrice* $\mathbf{\Phi}$, linking the state vector $\mathbf{Y}_k$ to $\mathbf{Y}_0$ as:

$$\mathbf{Y}_k = \mathbf{\Phi}\mathbf{Y}_0 \quad \text{with} \quad \mathbf{\Phi} = \mathbf{D}_{\mathbf{S},k-1}\mathbf{D}_{\mathbf{S},k-2}\ldots\mathbf{D}_{\mathbf{S},1}\mathbf{D}_{\mathbf{S},0} \tag{3.23}$$

The number of multiplications requiered to build $\mathbf{\Phi}$ is only dependent on the time discretization k. Whereas the size of the system is both dependent on time and spatial discretizations. These multiplications make the computational time of this method slightly larger than for Chebyshev collocation technique.

Finally, just like for Chebyshev collocation method, the stability analysis is based on wether the eigenvalues of the transition matrix $\mathbf{\Phi}$ are in modulus less than one.

3.4 Stability analysis of milling: 1-DoF

Before using SDM or Chebyshev collocation technique to compute the stability of the rod model, a 1-DoF milling process will be studied. The choice of parameters and results will be based on the articles [8, 19], and the MATLAB codes are based on the code presented in [18, 21] (see Appendix A). Let us consider a standard linear DDE model of the milling process [19]:

$$\ddot{v}(t) + 2\xi\omega_n\dot{v}(t) + \omega_n^2 v(t) = \frac{bK_s(t)}{m}[v(t-\tau) - v(t)] \tag{3.24}$$

where, $K_s(t)$ is the specific cutting force variation defined as:

$$K_s(t) = \sum_{j=1}^{N_t} g_j(t)[K_t\cos(\phi_j(t)) + K_n\sin(\phi_j(t))]\sin(\phi_j(t)) \tag{3.25}$$

and, $\phi_j(t)$ is the cutting angle of the jth tooth:

$$\phi_j(t) = \Omega t + j\frac{2\pi}{N_t} \tag{3.26}$$

Equation (3.24) is the variational system of Equation (2.9) around a τ-periodic solution written in the modal domain. The system's constant delay τ is defined by Equation (2.10), N_t is the number of teeth on the cutter, b is the depth of cut, Ω is the spindle rotating frequency and g_j is a screen function:

$$g_j(t) = \begin{cases} 1 & \text{if the } j\text{th tooth is in cut} \\ 0 & \text{otherwise} \end{cases} \tag{3.27}$$

By using a state vector $\mathbf{Z}^{\mathrm{T}}(t) = (v(t)\ \dot{v}(t))$, Equation (3.24) can be rewritten as a DDE of the form of Equation (3.1), with:

$$\mathbf{A} = \begin{bmatrix} 0 & 1 \\ -\omega_n^2 - \frac{bK_s(t)}{m} & -2\xi\omega_n \end{bmatrix}; \quad \mathbf{B} = \begin{bmatrix} 0 & 0 \\ \frac{bK_s(t)}{m} & 0 \end{bmatrix} \tag{3.28}$$

which are then discretized in the time domain as:

$$\mathbf{A}_i = \begin{bmatrix} 0 & 1 \\ -\omega_n^2 - \frac{bK_{s,i}}{m} & -2\xi\omega_n \end{bmatrix}; \quad \mathbf{B}_i = \begin{bmatrix} 0 & 0 \\ \frac{bK_{s,i}}{m} & 0 \end{bmatrix}; \quad K_{s,i} = \frac{1}{\Delta t}\int_{t_i}^{t_{i+1}} K_s(t)dt \tag{3.29}$$

Using parameters $m = 2.573$ Kg, $\xi = 0.0032$, $f_n = \omega_n/2\pi = 146.5$ Hz, $K_n = 2\cdot 10^8$ N/m^2 and $K_t = 5.5\cdot 10^8$ N/m^2, and based on the results of sections 3.2 and 3.3, we computed the following stability lobes diagrams in agreement with articles [8, 19]. In both cases we chose $k = 40$ discretization points for the SDM and Chebyshev nodes for the Chebyshev collocation method. The grid of parameters b and Ω is 300×300, and the number of teeth of the cutter is set to $N_t = 1$.

As depicted in Fig. 3.2 both methods reproduce precisely the results of cited references and give a good grasp of the stability domain of the milling operation. As explained in section 2.3, the SLD represents the limit of the system's stability, *i.e.*, all combinations of parameters (rotational speed and depth of cut) leading to a stable cut are situated under the lobes, and on the contrary, chatter occurs for combinations situated over the lobes. Even though there are differences between both methods, the general behavior of the system remains unchanged. Therefore, these methods can now be used to compute the stability of the rod model (section 4). As previously stated, the computational time of SDM is slightly larger than Chebyshev collocation technique. Therefore, the latter method will be used to compute the stability of the rod model in the next chapter.

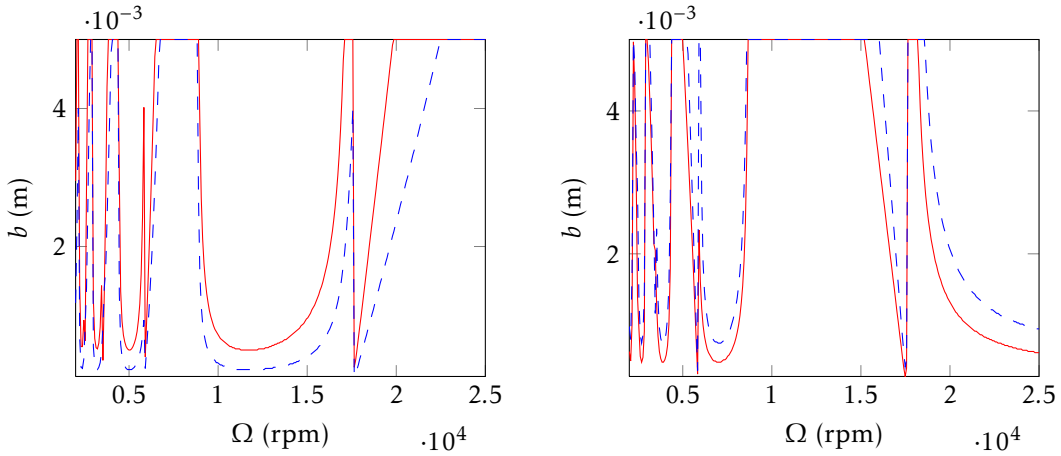

(a) Up-milling (b) Down-milling

Figure 3.2: SLD Milling 1DoF: Chebyshev Collocation (——), SDM (– –)

Chapter 4

Stability analysis of the rod model

This chapter features a stability analysis of the rod model built in chapter 1, using *Chebyshev collocation method* introduced in section 3.2. The MATLAB code for this analysis is given in Appendix B.

Instead of considering a casing profile as in the numerical model (section 1.2.2), a permanent contact configuration will be studied with a linear cutting force model. This will allow to model the system as a linear DDE defined by Eqs. (3.1) and (3.9) as shown in section 3.1.

After ensuring space and time convergence of the model, a modal analysis will enable to show each mode's contribution to the global dynamical behavior of the system, a parameter study will also be conducted, evaluating the influence of the damping, the stiffness and the mass of the rod regarding its stability. Finally, a numerical integration of the DDE will be done, using different set of parameters leading to stable and unstable behaviors, in order to check the consistency of the results.

4.1 Convergence of the model

In order to properly use the Chebyshev collocation method to study the stability of the system previously defined in section 3.1, space and time convergence should be checked. It is important to note that the space convergence is strictly dependent on the finite element model of the rod, *i.e.*, number of truss elements n. Whereas the time convergence is only dependent on the number of Chebyshev nodes k used for the discretization.

In this section, rotational frequencies f_Ω varying from 50 Hz to 250 Hz are considered, since this was the frequency range in which maximum wear phenomena were observed using the numerical model (section 1.5.1). As for the specific force coefficient K_e, it varies from $4.5 \cdot 10^4$ to $4.5 \cdot 10^6$ N/m^2.

4.1.1 Time convergence

The time convergence of the model is studied setting $n = 5$ truss elements in the finite element model of the rod. The number of Chebyshev nodes varies as $k = [20; 40; 60]$.

Figure 4.1 shows the time convergence of the model. As the number of Chebyshev nodes is increased, curves overlap perfectly (for $k = 40$ and $k = 60$).

As can also be seen in this figure, there is a major difference between the curves at low frequency ranges ($f_\Omega = [50; 80]$). Since the delay time τ is inversely proportional to

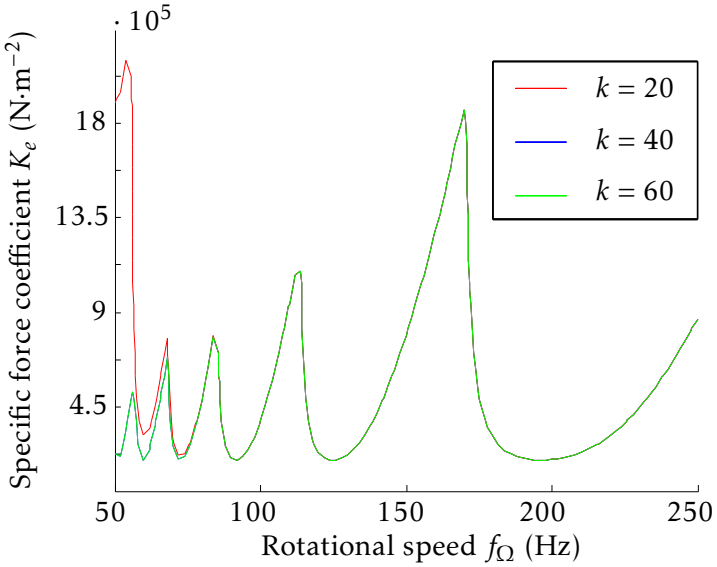

Figure 4.1: Time convergence

the rotational frequency, at low f_Ω a refinement of the time discretization is required to ensure the convergence.

Therefore, 40 Chebyshev collocation points will be enough to ensure the convergence of the solution.

4.1.2 Space convergence

Now that time convergence is ensured, k is set to 40 and the number of truss elements will vary so that $n = [2; 5; 10; 20]$. As shown in Figure 4.2, space convergence is quickly

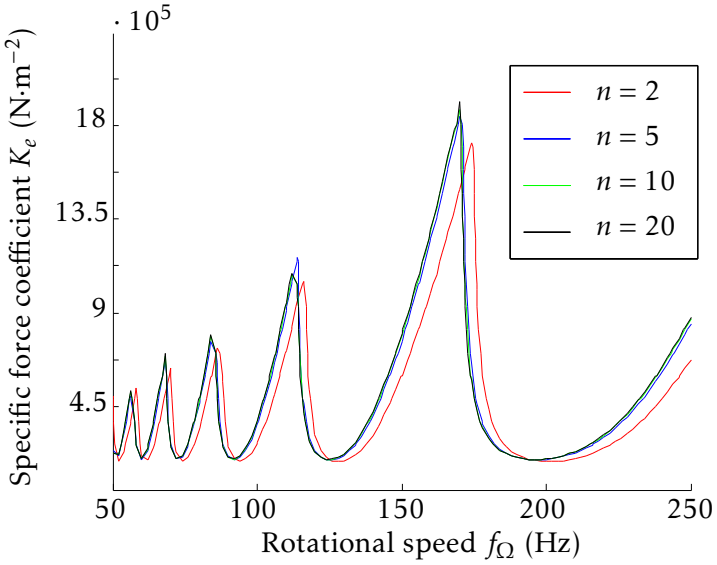

Figure 4.2: Space convergence

reached since there is no major difference between $n = 10$ and $n = 20$. Even for $n = 5$ a good accuracy is achieved, since the computational time is strongly dependent on the size of the system (matrices **A** and **B** of equation (3.1) are of size $2n \times 2n$), $n = 5$ will be used for the rest of the study.

4.2 Modal analysis

Before running any calculation regarding the contribution of each mode to the global behavior of the system, a more complete map of the rod's stability diagram is plotted in Figure 4.3. The range of rotational frequencies is $f_\Omega = [0;8,000]$ Hz and the specific force coefficient is $K_e = [4.5 \cdot 10^4; 13.5 \cdot 10^6]$ N/m^2. As shown in Figure 4.3, the stable

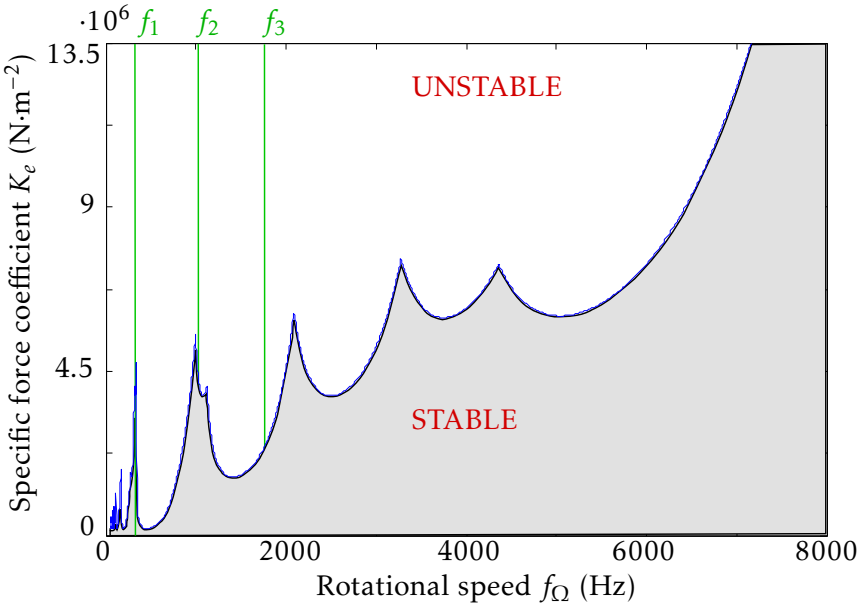

Figure 4.3: Global stability diagram

domain increases with the rotational frequency, which implies that the first mode of vibration is the most unstable one. This is in agreement with the chatter phenomenon observed in machining, where the chatter frequency is close to the natural frequency of a dominant structural mode of the system [1, 31]. Results presented in section 1.5.1 also confirm this statement, since no major vibrations are expected once the first eigenfrequency is passed.

To verify these statements, a calculation of the stability lobes was performed in order to separate each mode of the structure in equation (3.1). By selecting the appropriate rows of the eigenvectors $\mathbf{V}^T$ and columns of $\mathbf{V}$, one is able to isolate each mode's contribution to the global dynamical behavior of the system, *e.g.*, by reducing the system using the first two rows of $\mathbf{V}^T$ only modes 1 and 2 will be reflected in the diagram. Figure 4.4 validates the above statements. It clearly shows that global stability is driven by the stability of the first mode. The same observation can be made, if one considers only the first two modes of the structure instead of the global stability diagram.

This can be explained by the fact that the first mode of the rod is the most flexible one. Therefore, the divergence of the rod's response to a certain set of parameters is largely dependent on the first mode's behavior, *i.e.*, a set of parameters leading to a stable response if only the second mode is considered may lead to an unstable response if the first mode is taken into account, and consequently to a global unstable behavior.

Furthermore, Figure 4.5 not only shows the modal convergence of the model, but also that the higher modes have very small influence in the overall behavior of the system.

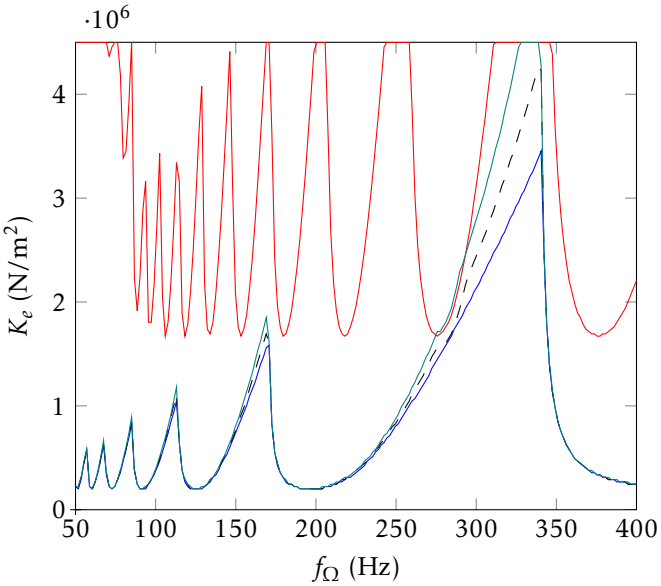

Figure 4.4: Modal contribution: Mode 1 (——), Mode 2 (——), Mode 1+2 (– –), Global stability (——)

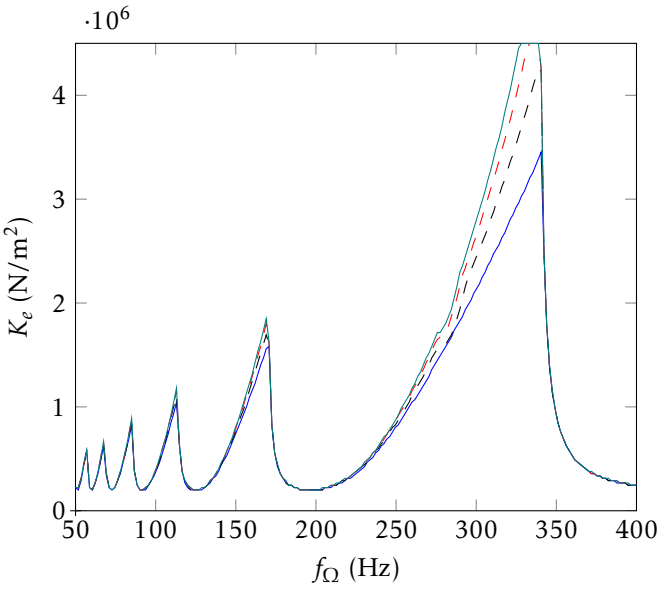

Figure 4.5: Modal convergence: Mode 1 (——), Modes 1+2 (– –), Mode 1 to 5 (– –), Global stability: Modes 1 to 15 (——)

4.3 Parameter analysis

As previously mentioned, the objective of this section is to analyze the influence of three different structural parameters of the rod: the stiffness (*i.e.*, Young Modulus E), the mass (*i.e.*, density ρ) and the damping coefficient ξ.

For each case, a color map will be computed showing the evolution of the stability lobes diagram as a function of the parameter of interest. A superposition of the stability lobes for different values of each parameter will also be drawn.

4.3.1 Stiffness

The first structural parameter studied is the rod's stiffness. This will represent de influence of the material's Young Modulus since the mass is constant. The variable stiffness will be defined as

$$\mathbf{K}' = \alpha \mathbf{K} \tag{4.1}$$

where α is a coefficient that will vary from 0.1 to 2, and $\mathbf{K}$ is the rod's stiffness defined in equation(1.4).

In this way, one is able to compute Figures 4.6 and 4.7. Figure 4.6 clearly shows

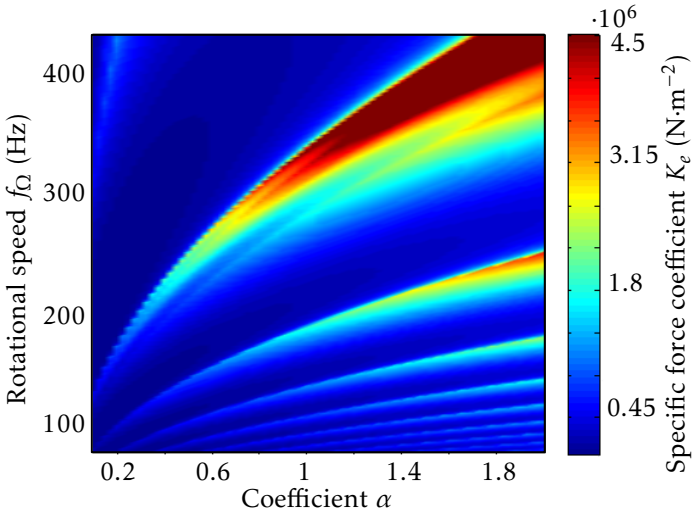

Figure 4.6: Influence of the rod's stiffness

the evolution of the stability lobes with a global expansion of each lobe as the stiffness and velocity are increased. Since the stiffness is linearly modified, there is a nonlinear evolution of the rod's eigenfrequencies, which explains the shape of the shift of the SLDs (evolution as a square rooted function). In addition to the lateral translation of

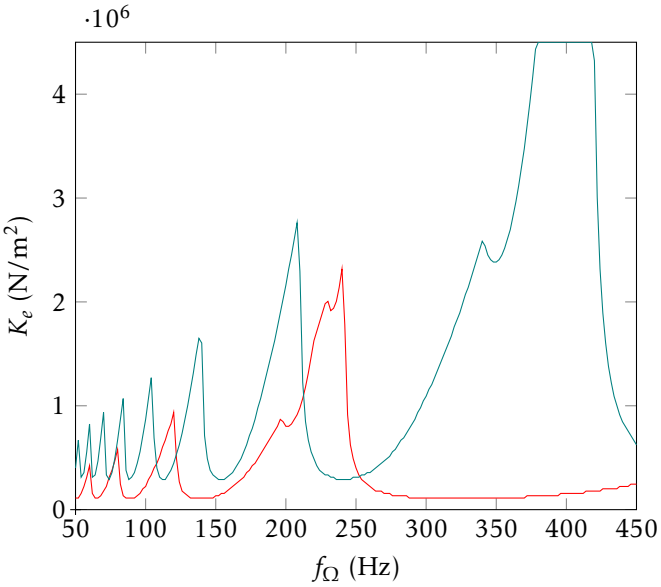

Figure 4.7: Influence of the rod's stiffness: $\alpha = 0.5$ (——), $\alpha = 1.5$ (——)

the lobes and the overall expansion, there is also an upward translation that can only be observed in Figure 4.7. This shift increases slightly the rod's stable domain.

4.3.2 Mass

The second structural parameter studied is the rod's mass. This will represent de influence of the material's density since the stiffness is kept constant. Just like in the previous section, a variable mass is defined as

$$\mathbf{M}' = \beta \mathbf{M} \tag{4.2}$$

where β is a coefficient that will vary from 0.1 to 2, and $\mathbf{M}$ is the rod's mass defined in equation(1.4).

The same kind of figures are then computed in Figs. 4.8 and 4.9. On the one hand,

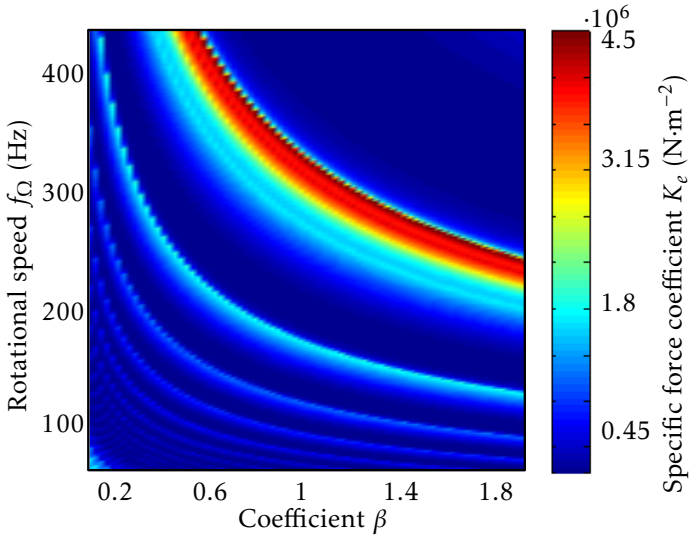

Figure 4.8: Influence of the rod's mass

just as for the stiffness, one can observe that the overall evolution of the lobes follow the nonlinear evolution of the eigenfrequencies in Figure 4.8 (inverse of a square rooted function). Therefore, the lobes are shifted to the left instead of to the right.

On the other hand, no vertical translation is shown in Figure 4.9 and consequently, no increase of the rod's stable domain. This indicates that the mass of the system only affects the position of the lobes but not their size.

4.3.3 Damping coefficient

The last parameter that will be studied is the damping coefficient ξ introduced in equation (1.9). It will vary from $\xi = 0$ (no structural damping) to $\xi = 0.05$ which is a range of values commonly used in the machining field.

Let us remind that this is a global damping coefficient that equally affects the contribution of all vibrational modes. Furthermore, since the damping does not affect the eigenfrequencies of the structure, no lateral shift should be observed in the lobes of the global stability chart. Figures 4.10 and 4.11 are in perfect agreement with the above statement, since no lateral shift of the lobes is observed. An expansion of the stable domain can also be seen as the damping coefficient is increased.

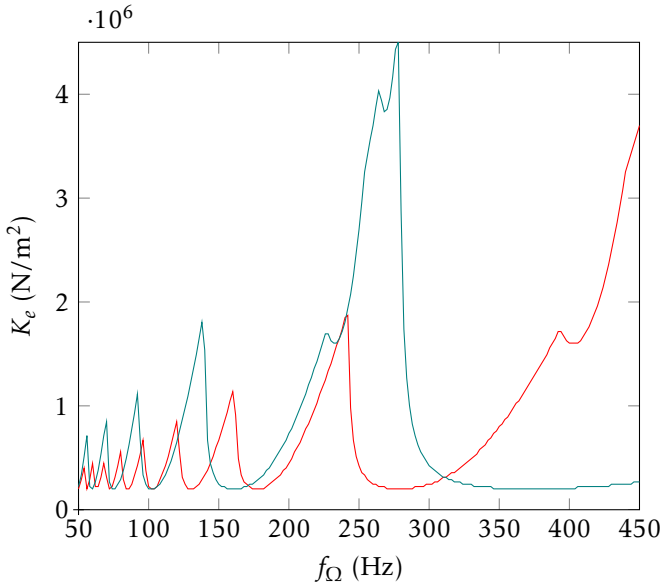

Figure 4.9: Influence of the rod's mass: $\beta = 0.5$ (——), $\beta = 1.5$ (——)

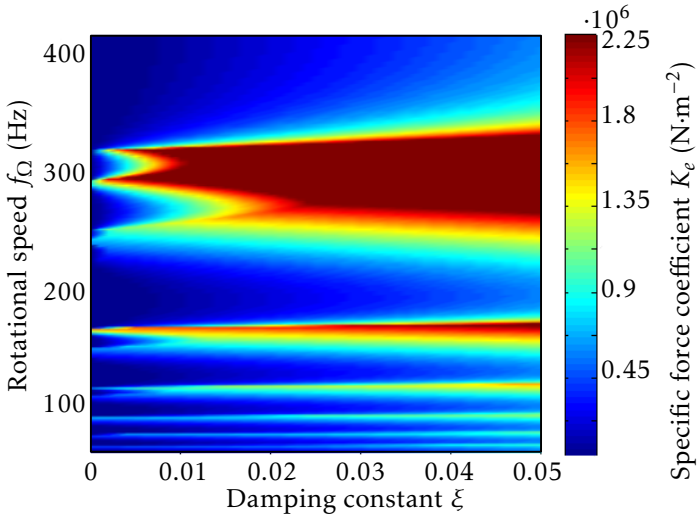

Figure 4.10: Influence of the rod's damping constant

4.4 Numerical integration of the DDE

The aim of this section is to use different sets of parameters obtained by the SLD leading both to stable and unstable behaviors, and numerically integrate the DDE in order to show that the rod's response converges or diverges respectively.

To do so, the structural parameters of the rod are kept constant: surface $S = 10 \cdot 10^{-4}$ m^2, length $L = 0.5$ m, Young's modulus $E = 210 \cdot 10^7$ Pa, density $\rho = 4600$ Kg/m^3 and damping constant $\xi = 0.03$.

As for the rotational frequency and the specific force coefficient, for $f_\Omega = 85$ Hz and $f_\Omega = 112$ Hz, both $K_e = 4.5 \cdot 10^5$ N/m^2 and $K_e = 1.35 \cdot 10^6$ N/m^2 were tested. As shown in Figure 4.12 these combinations of parameters should lead both to stable and unstable responses. For the numerical integration, the same algorithm described in section 1.4 was used, the only difference being that the contact force is based on the blade's tip position at the preceding revolution instead of the casing's shape.

The computational parameters are:

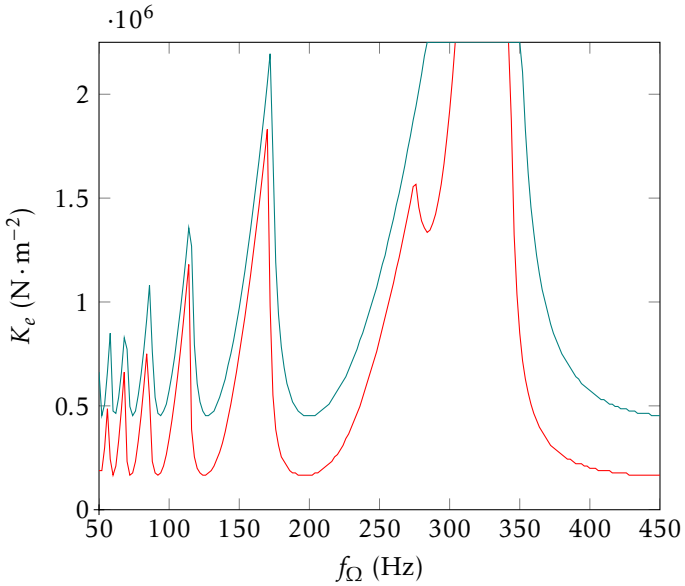

Figure 4.11: Influence of the rod's damping constant: $\xi = 0.015$ (——), $\xi = 0.04$ (——)

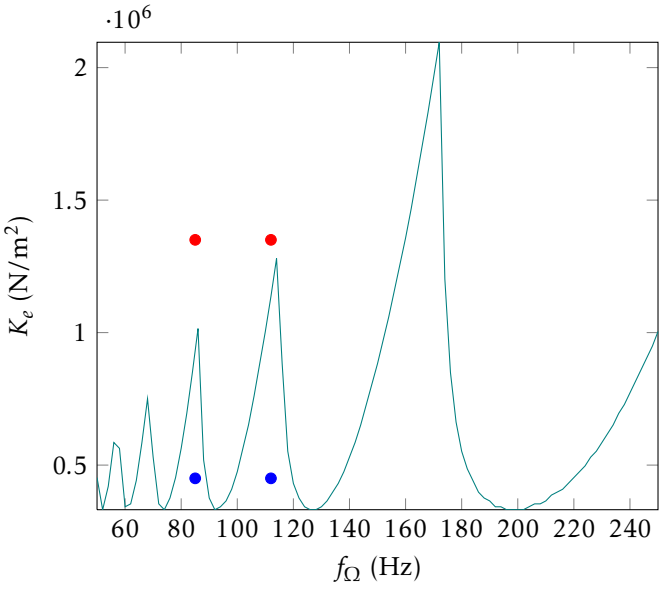

Figure 4.12: Stable parameters (—●—); Unstable parameters (—●—)

- Finite element model of the rod: $n = 5$ truss elements
- Finite difference time step: $\Delta t = 1 \cdot 10^{-6}$ s
- Total time: 10 revolutions

As previously stated, in order to solve a DDE as in equation (3.1), an initial function covering the period $[-\tau\,;0]$ must be defined. In this particular case, it will allow to initiate the contact, therefore, a slowly growing function was defined for the first revolution such as:

$$\begin{aligned} &\mathbf{q}(0) = \begin{pmatrix} 0 & 0.2 \cdot 10^{-7} & 0.4 \cdot 10^{-7} & 0.6 \cdot 10^{-7} & 0.8 \cdot 10^{-7} & 1 \cdot 10^{-7} \end{pmatrix} \\ &\mathbf{q}(t + dt) = 1.0005\mathbf{q}(t) \quad \text{with} \quad t \in [0\,;\tau] \end{aligned} \tag{4.3}$$

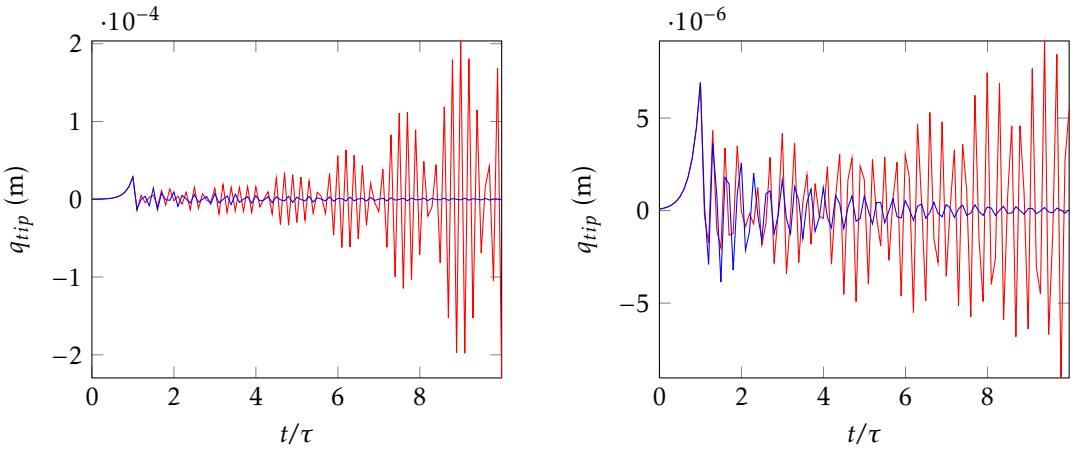

(a) $f_\Omega = 85$ Hz (b) $f_\Omega = 112$ Hz

Figure 4.13: Tip displacement: $K_e = 4.5 \cdot 10^5$ N · m^{-2} Stable (——); $K_e = 1.35 \cdot 10^5$ N · m^{-2} Unstable (——)

Results shown in Figure 4.13 prove that the SLD drawn in Figure 4.12 is conclusive regarding the stability prediction of the system. Both stable and unstable responses are observed with the corresponding set of parameters.

A large difference between Figs. 4.13a and 4.13b is observed in terms of the displacement's amplitude of the divergent solution. This can be explained by the fact that the choice of parameters is much closer to the stable domain for $f_\Omega = 112$ Hz than for $f_\Omega = 85$ Hz, consequently leading to a more abrupt increase of oscillations in the latter case.

Conclusions

The first chapter allowed us to point out several important dynamic behaviors of the rod-like blade model, similar to those presented in previous work [2, 3, 24], using time integration techniques such as:

- Influence of the so-called engine orders
- Appearance of critical frequencies and contact stiffening
- The lobe wear patterns that are produced in the abradable layer after a certain number of revolutions
- Once the first eigenfrequency is passed, no major vibrations are expected.

The system was then modeled by a set of DDEs by considering a permanent contact configuration. The model was based on the mathematical tools used in the high speed machining field and allowed to perform a global stability analysis of the system, which is impossible with more complex models that can only be treated with time integration techniques.

Both Chebyshev collocation technique and Semi-Discretization Method were used, showing that the difference in computational time between the two methods would be significant for systems with important delays or higher degrees of freedom. A parameter study was also conducted to evaluate the influence of rod's stiffness, mass and modal damping on its stability.

This global stability analysis also pointed out the fact that the system's stability is mostly driven by the stability of the first mode of the structure, which is consistent with the observations made with the numerical model.

Both models are based on an oversimplified model of the blade and only take into account the radial displacement, while flexural displacement may have a significant contribution in the dynamical behavior of the blades and the wear phenomenon.

Therefore, a more complex finite element model of the blade should be introduced. Further work can also be done regarding the modeling of the abradable layer by considering a flexible casing, which would enable to study the mode coupling between blade and casing.

Finally, other types of contact laws may be introduced in order to consider nonlinear models.

Appendix A

One degree-of-freedom milling: Semi-Discretization Method

The code presented in this appendix is mostly based on [18].

```
%%%%%%%%%%%%%%%%%%%%%%%%%%%%%%%
%%%%%%%%% Parameters %%%%%%%%%%
%%%%%%%%%%%%%%%%%%%%%%%%%%%%%%%
N=1;              % Number of teeth
Kt=5.5e8;         % Tangential cutting force coefficient (N/m2)
Kn=2e8;           % Normal cutting force coefficient (N/m2)
w0=146.5*2*pi;    % Angular natural frequency (rad/s)
zeta=0.0032;      % Relative damping
m_t=2.573;        % Mass (kg)
aD=0.5;           % Radial depth of cut ratio

%%%%%%%%%%%%%%%%%%%%%%%%%%%%%%%
%%% Type of milling process %%%
%%%%%%%%%%%%%%%%%%%%%%%%%%%%%%%
up_or_down=-1;       % 1: up-milling, -1: down-milling
if up_or_down==1
    fist=0;               % start angle
    fiex=acos(1-2*aD);    % exit angle
elseif up_or_down==-1
    fist=acos(2*aD-1);    % start angle
    fiex=pi;              % exit angle
end

%%%%%%%%%%%%%%%%%%%%%%%%%%%%%%%
%%% Computational parameters %%%
%%%%%%%%%%%%%%%%%%%%%%%%%%%%%%%
stx=300;          % Steps of spindle speed
o_st=2e3;         % Starting spindle speed (rpm)
o_fi=25e3;        % Final spindle speed (rpm)
sty=300;          % Steps of depth of cut
w_st=0e-3;        % Starting depth of cut (m)
w_fi=5e-3;        % Final depth of cut (m)
k=40;             % number of discretization interval over one period
k2=20;            % number of numerical integration steps for cutting force
```

```
m=k;              % since time delay = time period
% Weighted linear combination of the delay term
wa=1/2; wb=1/2;
D_S=zeros(m+2,m+2);     % matrix D_S (Discrete map)
d=ones(m+1,1);
d(1:2)=0;               % No delay term in speed
D=D+diag(d,-1);
D(3,1)=1;

%%%%%%%%%%%%%%%%%%%%%%%%%%%%%%%%%%%%%%%%%%%%%%%%%%%%%%%%%%%%
% Integration of specific cutting force coefficient %
%%%%%%%%%%%%%%%%%%%%%%%%%%%%%%%%%%%%%%%%%%%%%%%%%%%%%%%%%%%%
K_s=zeros(k,1);       % Specific force coefficient
for i=1:k
     dtr=2*pi/k;    % Angular step
     for j=1:N    % loop for tooth j
          fi=zeros(k2,1);    % Cutting angle
          g=zeros(k2,1);     % Screen function
          for h=1:k2  % loop for numerical integration of K_s
              fi(h)=(i-1)*dtr+(j-1)*2*pi/N+h*dtr/k2;
              if fi(h)>2*pi
                  fi(h)=fi(h)-2*pi;
              end
              if (fi(h)>=fist)&&(fi(h)<=fiex)
                   g(h)=1;  % tooth is in the cut
              else
                   g(h)=0;  % tooth is out of cut
              end
          end
          K_s(i)=K_s(i)+sum(g.*(Kt.*cos(fi)+Kn.*sin(fi)).*sin(fi))/k2;
     end
end

%%%%%%%%%%%%%%%%%%%%%%%%%%%%
%%% Start of computation %%%%
%%%%%%%%%%%%%%%%%%%%%%%%%%%%
EI=zeros(stx+1,1);  % Eigenvalues of transition matrix
SS=zeros(stx+1,1);  % Spindle speeds
DC=zeros(stx+1,1);  % Depths of cut
for x=1:stx+1       % loop for spindle speeds
     o=o_st+(x-1)*(o_fi-o_st)/stx;    % Spindle speed
     tau=60/o/N;    % time delay
     dt=tau/m;      % time step
     for y=1:sty+1       % loop for depth of cuts
        w=w_st+(y-1)*(w_fi-w_st)/sty;    % depth of cut
        % Construction of transition matrix Fi
        Fi=eye(m+2, m+2);
        for i=1:m     % loop for time discretization
             A=zeros(2, 2);                % matrix Ai
             A(1,2)=1;
```

```
            A(2,1)=-w0^2-h_i(i)*w/m_t;
            A(2,2)=-2*zeta*w0;
            B=zeros(2, 2);                % matrix Bi
            B(2,1)=h_i(i)*w/m_t;
            P=expm(A*dt);                 % matrix Pi
            R=(expm(A*dt)-eye(2))*(A\B); % matrix Ri
            D_S(1:2,1:2) = P;
            D_S(1:2,m+1) = wa*R(1:2, 1:1);
            D_S(1:2,m+2) = wb*R(1:2, 1:1);
            Fi=D*Fi;                      % Transition matrix
        end
        ei=max(abs(eig(Fi))); % Maximum of eigenvalues of Fi
        if ei>=1     % Limit of stability
            EI(x)=ei;
            SS(x)=o;     % Critical spindle speed
            DC(x)=w;     % Critical depth of cuts
            break
        end
        if w==w_fi   % Unstable domain is not reached
            EI(x)=1;
            SS(x)=o;
            DC(x)=w_fi;
        end
    end
    stx+1-x
end

%%%%%%%%%%%%%%%%%%%%%%%%%%%%%%%%%%
%%%%%%%%%% Plot figure %%%%%%%%%%
%%%%%%%%%%%%%%%%%%%%%%%%%%%%%%%%%%
figure(1);
plot(SS,DC,'b');
xlabel('Spindle speed (Hz)')
ylabel('Depth of cut (m)')

%%%%%%%%%%%%%%%%%%%%%%%%%%%%%%%%%%
%%%%%%%%% Save results %%%%%%%%%%
%%%%%%%%%%%%%%%%%%%%%%%%%%%%%%%%%%
file=['results_SDM_1dof_mill_down.mat'];
save(file,'SS','DC','EI');
```

Appendix B

Rod model: Chebyshev Collocation Method

The code presented in this appendix is mostly based on [8].

```
%%%%%%%%%%%%%%%%%%%%%%%%%%%%
%%%%% Rod parameters %%%%%%%
%%%%%%%%%%%%%%%%%%%%%%%%%%%%
rho=4600;   % Density (Kg/m3)
L=0.5;      % Length (m)
S=10e-4;    % Cross-section (m2)
E=210e7;    % Young Modulus (Pa)

%%%%%%%%%%%%%%%%%%%%%%%%%%%%%%%%%%%%
%%% Finite element discretization %%%
%%%%%%%%%%%%%%%%%%%%%%%%%%%%%%%%%%%%
n_el=5;      % Number of truss elements
le=L/n_el;   % Elementary length (m)
ki=E*S/le;   % Elementary stiffness (N/m)
mi=rho*S*le; % Elementary mass (Kg)

% Construction of stiffness and mass matrices
% Elementary matrices
A=zeros(n_el+1,n_el+1);  % Mass
B=zeros(n_el+1,n_el+1);  % Stiffness
Ae=[2 1;1 2];
Be=[1 -1;-1 1];

% Global matrices
for i=1:n_el;
    A(i:i+1,i:i+1)=A(i:i+1,i:i+1)+Ae;
    B(i:i+1,i:i+1)=B(i:i+1,i:i+1)+Be;
end
M=mi/6*A;       % Global mass matrix
K=ki*B;         % Global stiffness matrix

% Boundary conditions: first node clampsed
Mr=M(2:end,2:end);
Kr=K(2:end,2:end);
```

```
n=length(Kr);                              % Size of the DDE system

% Construction of damping matrix
[V,Lambda]=eig(Kr,Mr);                     % Eigenquantities
fei=sqrt(diag(Lambda))/2/pi;               % Eigenfrequencies
ksi=0.0177;                                % Single damping constant
C=2*ksi*(V')^(-1)*sqrt(Lambda)*V^(-1); % Damping matrix

%%%%%%%%%%%%%%%%%%%%%%%%%%%%%%%%
%%% Computational parameters %%%
%%%%%%%%%%%%%%%%%%%%%%%%%%%%%%%%
Force_s=zeros(n,n);  % Force matrix
stx=350;             % Steps of rotational speed
o_st=50;             % Starting rotational speed (Hz)
o_fi=400;            % Final rotational speed (Hz)
sty=400;             % Steps of specific force coefficient
Kn_st=4.5e4;         % Starting specific force coefficient (N/m2)
Kn_fi=4.5e6;         % Final specific force coefficient (N/m2)
m=40;                % number of Chebyshev nodes over one period
EI=zeros(stx+1,1);   % Monodromy operator eigenvalues
F_o=zeros(stx+1,1);  % Rotational frequency
Kn_c=zeros(stx+1,1); % Critical specific force coefficient

%%%%%%%%%%%%%%%%%%%%%%%%%%
%%%%%% Simulation %%%%%%
%%%%%%%%%%%%%%%%%%%%%%%%%%
for x=1:stx+1 % loop for rotational speeds
     o=o_st+(x-1)*(o_fi-o_st)/stx;   % spindle speed (Hz)
     tau=1/o;                        % time delay
     % Chebyshev polynomials scaled to the interval [-tau,0]
     DD=cheb(m-1)*2/tau;
     % Differentiation matrix
     DN=kron([DD(1:end-1,:);[zeros(1,m-1),1]],eye(2*n));
     for y=1:sty+1 % loop for depth of cuts
          Kn=Kn_st+(y-1)*(Kn_fi-Kn_st)/sty; % Specific force
          % Construction of monodromy operator U
          Force_s(end,end)=Kn;
          kappa=V'*Force_s*V;  % Specific force in modal domain
          A=zeros(2*n,2*n);    % matrix A
          A(1:n,n+1:2*n) = eye(n);
          A(n+1:2*n,1:n) =-Lambda-kappa;
          A(n+1:2*n,n+1:2*n) =-2*ksi*sqrt(Lambda);
          % matrix MA
          MA=kron([eye(m-1,m);zeros(1,m)],A);
          B=zeros(2*n,2*n);    % matrix B
          B(n+1:2*n,1:n) = kappa;
          % matrix MB
          MB=[kron([eye(m-1,m)],B);kron([1,zeros(1,m-1)],eye(2*n))];
          U=(DN-MA)\MB;        % Monodromy operator
          ei=max(abs(eig(U)))
```

```
            if ei>=1      % Limit of stability
                EI(x)=ei;
                F_o(x)=o;      % Critical rotational frequency
                Kn_c(x)=Kn;    % Critical specific force coefficient
                break
            end
            if w==w_fi    % Unstable domain is not reached
                EI(x)=1;
                F_o(x)=o;
                Kn_c(x)=Kn_fi;
            end
        end
        stx+1-x
end

%%%%%%%%%%%%%%%%%%%%%%%%%%%%%%%%%%
%%%%%%%%% Plot figure %%%%%%%%%%
%%%%%%%%%%%%%%%%%%%%%%%%%%%%%%%%%%
figure(1); hold on;
plot(F_o,Kn_c,'b');
xlabel('Rotational frequency (Hz)')
ylabel('Specific force coefficient (N/m2)')

%%%%%%%%%%%%%%%%%%%%%%%%%%%%%%%%%%
%%%%%%%%% Save results %%%%%%%%%%
%%%%%%%%%%%%%%%%%%%%%%%%%%%%%%%%%%
file=['results_stab_rod_.mat'];
save(file,'F_o','Kn_c','EI','fpropres');
```

References

[1] Y. Altintas. *Manufacturing Automation: Metal Cutting Mechanics, Machine Tool Vibrations, and CNC Design*. Cambridge University Press, 2000. ISBN: 0-5216-5973-6 (p. 39).

[2] A. Batailly, M. Legrand, and C. Pierre. "Influence of Abradable Coating Wear Mechanical Properties on Rotor Stator Interaction". *Proceedings of the ASME Turbo Expo*. 2011 (pp. 5, 9, 11, 18, 47).
oai:hal.archives-ouvertes.fr:hal-00616524.

[3] A. Batailly, M. Legrand, C. Pierre, and B. Magnain. "Validation d'un algorithme de contact 3D utilisé pour l'étude de contacts aube/carter dans les turbomachines aéronautiques". *8th International Conference on Rotor Dynamics IFToMM*. Sept. 2010 (pp. 5, 9, 11, 18, 47).
oai:hal.archives-ouvertes.fr:hal-00533382.

[4] P. Bayly, J. Halley, B. Mann, and M. Davies. "Stability of Interrupted Cutting by Temporal Finite Element Analysis". *Journal of Manufacturing Science and Engineering* 125.2 (2003), pp. 220–225 (p. 26).
DOI: 10.1115/1.1556860.

[5] Ed Bueler. "Error Bounds for Approximate Eigenvalues of Periodic-Coefficient Linear Delay Differential Equations". *SIAM Journal on Numerical Analysis* 45.6 (2007), pp. 2510–2536 (p. 31).
DOI: DOI:10.1137/050633330.

[6] E. Butcher, O. Bobrenkov, E. Bueler, and P. Nindujarla. "Analysis of Milling Stability by the Chebyshev Collocation Method: Algorithm and Optimal Stable Immersion Levels". *Journal of Computational and Nonlinear Dynamics* 4.3 (2009) (p. 31).
DOI: 10.1115/1.3124088.

[7] E. Butcher, H. Ma, E. Bueler, V. Averina, and Z. Szabo. "Stability of linear time-periodic delay-differential equations via Chebyshev polynomials". *International Journal for Numerical Methods in Engineering* 59 (2004), pp. 895–922 (p. 31).
DOI: 10.1002/nme.894.

[8] E. Butcher, P. Nindujarla, and E. Bueler. "Stability of Up- and Down-Milling Using Chebyshev Collocation Method". *ASME Conference Proceedings* 2005.47438 (2005), pp. 841–850 (pp. 31, 32, 34, 53).
DOI: 10.1115/DETC2005-84880.

[9] N. Corduan. "Étude des phénomènes vibratoires en fraisage de finition de plaques minces : application aux aubages de turbines aéronautiques". PhD Thesis. École Nationale des Arts et Métiers, 2006 (p. 21).
oai:pastel.archives-ouvertes.fr:pastel-00002483.

[10] N. Deshpande and M. Fofana. "Nonlinear regenerative chatter in turning". *Robotics and Computer Integrated Manufacturing* 17 (2001), pp. 107–112 (p. 26).
DOI: 10.1016/S0736-5845(00)00043-0.

[11] O. Diekmann, S.A. van Giles, S.M. Verduyn Lunel, and H.O. Walther. *Delay Equations: Functional-, Complex-, and Nonlinear Analysis*. Springer-Verlag Berlin and Heidelberg GmbH & Co. KG, 1995. ISBN: 0-3879-4416-8 (p. 29).

[12] Z. Dombovari, D. Barton, R. Wilson, and G. Stepan. "On the global dynamics of chatter in the orthogonal cutting model". *International Journal of Non-Linear Mechanics* 46 (2011), pp. 330–338 (pp. 21, 25).
DOI: 10.1016/j.ijnonlinmec.2010.09.016.

[13] R. Faassen, N. van de Wouw, J. Oosterling, and H. Nijmeijer. "Prediction of regenerative chatter by modelling and analysis of high-speed milling". *International Journal of Machine Tools & Manufacture* 43 (2003), pp. 1437–1446 (p. 22).
DOI: 10.1016/S0890-6955(03)00171-8.

[14] V. Gagnol, B. Bouzgarrou, P. Ray, and C. Barra. "Model-based chatter stability prediction for high-speed spindles". *International Journal of Machine Tools & Manufacture* 47 (2007), pp. 1176–1186 (p. 21).
DOI: 10.1016/j.ijmachtools.2006.09.002.

[15] J. Hung, Y. Lai, and H. You. "Finite Element Prediction on the Machining Stability of Milling Machine with Experimental Verification". *World Academy of Science, Engineering and Technology* 72 (2010) (p. 26).
URL: http://www.waset.org/journals/waset/v72/v72-40.pdf.

[16] T. Insperger. "Stability Analysis of Periodic Delay-Differential Equations Modeling Machine Tool Chatter". PhD Thesis. Budapest University of Technology and Economics, 2002 (pp. 26, 32).
URL: http://www.mm.bme.hu/~inspi/dissert.pdf.

[17] T. Insperger and G. Stepan. "Semi-discretization method for delayed systems". *International Journal for Numerical Methods in Engineering* 55 (2002), pp. 503–518 (pp. 32, 33).
DOI: 10.1002/nme.505.

[18] T. Insperger and G. Stepan. "Updated semi-discretization method for periodic delay-differential equations with discrete delay". *International Journal for Numerical Methods in Engineering* 61 (2004), pp. 117–141 (pp. 32–34, 49).
DOI: 10.1002/nme.1061.

[19] T. Insperger, G. Stepan, B. Mann, and P. Bayly. "Stability of up-milling and down-milling, part 1: alternative analytical methods". *International Journal of Machine Tools & Manufacture* 43 (2003), pp. 25–34 (pp. 21, 34).
DOI: 10.1016/S0890-6955(02)00159-1.

[20] T. Insperger, G. Stepan, and J. Turi. "State-dependent delay in regenerative turning processes". *Nonlinear Dynamics* 47 (2007), pp. 275–283 (pp. 22, 26).
DOI: 10.1007/s11071-006-9068-2.

[21] E. Jarlebring. "The spectrum of delay-differential equations: numerical methods, stability and perturbation". PhD Thesis. Technische Universität Carolo-Wilhelmina zu Braunschweig, 2008 (pp. 29, 34).
URL: people.cs.kuleuven.be/~elias.jarlebring/doc/thesis-final.pdf.

[22] M. Lakshmanan and D. Senthilkumar. "Dynamics of Nonlinear Time-Delay Systems". Springer-Verlag, 2010. Chap. 1 and 2, pp. 1–29. ISBN: 3-6421-4937-5 (p. 29).

[23] Mathias Legrand. "Modèles de prédiction de l'interaction rotor/stator dans un moteur d'avion". PhD thesis. Université de Nantes, 2005 (p. 11).
oai:tel.archives-ouvertes.fr:tel-00011631.

[24] M. Legrand and C. Pierre. "Numercial Investigation of Abradable Coating Wear through Plastic Constitutive Law: Application to Aircraft Engines". *International Design Engineering Technical Conferences & Computers and Information in Engineering Conference*. 2009 (pp. 5, 9, 11, 18, 47).
oai:oai:hal.archives-ouvertes.fr:hal-00413728.

[25] H. Li, X. Li, and X. Chen. "A novel chatter stability criterion for the modelling and simulation of the dynamic milling process in the time domain". *International Journal of Advanced Manufacturing Technology* 22 (2003), pp. 619–625 (p. 26).
DOI: 10.1007/S00170-003-1562-9.

[26] X. Li, A. Nee, Y. Wong, and H. Zheng. "Theoretical modelling and simulation of milling forces". *Journal of Materials Processing Technology* 89 (1999), pp. 266–272 (p. 21). DOI: 10.1016/S0924-0136(99)00076-X.

[27] I. Mane, V. Gagnol, B. Bouzgarrou, and P. Ray. "Stability-based spindle speed control during flexible workpiece high-speed milling". *International Journal of Machine Tools & Manufacture* 48 (2008), pp. 184–194 (p. 26). DOI: 10.1016/j.ijmachtools.2007.08.018.

[28] M. Merchant. "Mechanics of the Metal Cutting Process. II. Plasticity Conditions in Orthogonal Cutting". *Journal of Applied Physics* 16.6 (June 1945), pp. 318–324 (p. 21). DOI: 10.1063/1.1707596.

[29] M. Merchant. "Mechanics of the Metal Cutting Process. I. Orthogonal Cutting and a Type 2 Chip". *Journal of Applied Physics* 16 (May 1945), pp. 267–275 (p. 21). DOI: 10.1063/1.1707586.

[30] W. Michiels and S-I. Niculescu. "Stability and Stabilization of Time-Delay Systems". Society for Industrial and Applied Mathematics, 2007. Chap. 1 and 6, ISBN: 0-8987-1632-2 (p. 29).

[31] Z. Pan, H. Zhang, Z. Zhu, and J. Wang. "Chatter analysis of robotic machining process". *Journal of Materials Processing Technology* 173.3 (2006), pp. 301 –309 (p. 39). DOI: 10.1016/j.jmatprotec.2005.11.033.

[32] J-P. Richard, H. Mounier, A. Achour, L. Belkoura, S. Ben Attia, M. Dambrine, M. Ksouri, W. Perruquetti, J. Rudolph, S. Salhi, and F. Woittennek. "Mathématiques pour l'ingénieur". 2009. Chap. 6, pp. 235–277 (p. 29). oai:hal.archives-ouvertes.fr:hal-00519555.

[33] T. Schmitz and K. Smith. "Machining Dynamics". Springer Science+Business Media, 2009. Chap. 3 and 4, pp. 59–170. ISBN: 0-3870-9644-2 (p. 22).

[34] S. Seguy. "De l'adaptation à la variation continue de la vitesse de broche afin de contrôler le broutement en fraisage de parois minces : modélisations et études expérimentales". PhD Thesis. Institut National Polytechnique de Toulouse, 2008 (p. 26). oai:tel.archives-ouvertes.fr:tel-00374725.

[35] R. Seydel. *Practical Bifurcation and Stability Analysis*. Springer Science+Business Media, 2010. ISBN: 1-4419-1739-3 (p. 29).

[36] G. Stepan. "Modelling Nonlinear Regenerative Effects in Metal Cutting". *Philosophical Transactions: Mathematical, Physical and Engineering Sciences* 359 (2001), pp. 739–757 (p. 26). URL: http://www.jstor.org/stable/3066408.

[37] G. Stepan, R. Szalai, B. Mann, P. Bayly, T. Insperger, J. Gradisek, and E. Govekar. "Nonlinear Dynamics of High-Speed Milling—Analyses, Numerics, and Experiments". *Journal of Vibration and Acoustics* 127.2 (2005), pp. 197–203 (pp. 22, 26). DOI: 10.1115/1.1891818.

[38] W. Tang, Q. Song, S. Yu, S. Sun, B. Li, B. Du, and X. Ai. "Prediction of chatter stability in high-speed finishing end milling considering multi-mode dynamics". *Journal of Materials Processing Technology* 209 (2009), pp. 2585–2591 (p. 26). DOI: 10.1016/j.jmatprotec.2008.06.003.

[39] G. Tlusty. *Manufacturing Processes and Equipment*. Prentice Hall, 2000. ISBN: 0-2014-9865-0 (pp. 21, 22, 25, 26).

[40] J. Tlusty and M. Polacek. "The stability of the machine tool against self-excited vibration in machining". *International Research in Production Engineering* (1963), pp. 465–474 (p. 23).

[41] S. Tobias. *Machine-tool vibration ; authorized translation by A.H. Burton*. London: Blackie, 1965 (p. 23).

[42] L. Trefethe. *Spectral Methods in MATLAB*. Society for Industrial and Applied Mathematics, 2000. ISBN: 0-8987-1465-6 (p. 31).

[43] T. Vyhlídal. "Analysis and Synthesis of Time Delay System Spectrum". PhD Thesis. Czech Technical University in Prague, 2003 (p. 29).
URL: http://www.cak.fs.cvut.cz/old/Dokumenty/autoref.pdf.

[44] X. Zhang, C. Xiong, and Y. Ding. "Improved Full-Discretization Method for Milling Chatter Stability Prediction with Multiple Delays". *International Conference on Intelligent Robotics and Applications*. 2010, pp. 541–552. ISBN: 3-6421-6586-9 (p. 26).
URL: http://portal.acm.org/citation.cfm?id=1939525.1939582.